doi:10.3847/0067-0049/224/1/1

THE REDMAPPER GALAXY CLUSTER CATALOG FROM DES SCIENCE VERIFICATION DATA

E. S. Rykoff[1,2], E. Rozo[3], D. Hollowood[4], A. Bermeo-Hernandez[5], T. Jeltema[4], J. Mayers[5], A. K. Romer[5], P. Rooney[5], A. Saro[6], C. Vergara Cervantes[5], R. H. Wechsler[1,2,7], H. Wilcox[8], T. M. C. Abbott[9], F. B. Abdalla[10,11], S. Allam[12], J. Annis[12], A. Benoit-Lévy[10,13,14], G. M. Bernstein[15], E. Bertin[13,14], D. Brooks[10], D. L. Burke[1,2], D. Capozzi[8], A. Carnero Rosell[16,17], M. Carrasco Kind[18,19], F. J. Castander[20], M. Childress[21,22], C. A. Collins[23], C. E. Cunha[1], C. B. D'Andrea[8,24], L. N. da Costa[16,17], T. M. Davis[25], S. Desai[26,6], H. T. Diehl[12], J. P. Dietrich[26,6], P. Doel[10], A. E. Evrard[27,28], D. A. Finley[12], B. Flaugher[12], P. Fosalba[20], J. Frieman[12,29], K. Glazebrook[30], D. A. Goldstein[31,32], D. Gruen[1,2,33,34], R. A. Gruendl[18,19], G. Gutierrez[12], M. Hilton[35], K. Honscheid[36,37], B. Hoyle[34], D. J. James[9], S. T. Kay[38], K. Kuehn[39], N. Kuropatkin[12], O. Lahav[10], G. F. Lewis[40], C. Lidman[39], M. Lima[16,41], M. A. G. Maia[16,17], R. G. Mann[42], J. L. Marshall[43], P. Martini[36,44], P. Melchior[45], C. J. Miller[27,28], R. Miquel[46,47], J. J. Mohr[26,6,33], R. C. Nichol[8], B. Nord[12], R. Ogando[16,17], A. A. Plazas[48], K. Reil[2], M. Sahlén[49], E. Sanchez[50], B. Santiago[16,51], V. Scarpine[12], M. Schubnell[28], I. Sevilla-Noarbe[18,50], R. C. Smith[9], M. Soares-Santos[12], F. Sobreira[12,16], J. P. Stott[49], E. Suchyta[15], M. E. C. Swanson[19], G. Tarle[28], D. Thomas[8], D. Tucker[12], S. Uddin[30], P. T. P. Viana[52,53], V. Vikram[54], A. R. Walker[9], and Y. Zhang[28]

(The DES Collaboration)

[1] Kavli Institute for Particle Astrophysics & Cosmology, P.O. Box 2450, Stanford University, Stanford, CA 94305, USA; erykoff@slac.stanford.edu
[2] SLAC National Accelerator Laboratory, Menlo Park, CA 94025, USA
[3] Department of Physics, University of Arizona, Tucson, AZ 85721, USA
[4] Department of Physics and Santa Cruz Institute for Particle Physics, University of California, Santa Cruz, CA 95064, USA
[5] Department of Physics and Astronomy, Pevensey Building, University of Sussex, Brighton, BN1 9QH, UK
[6] Faculty of Physics, Ludwig-Maximilians University, Scheinerstrasse 1, D-81679 Munich, Germany
[7] Department of Physics, Stanford University, 382 Via Pueblo Mall, Stanford, CA 94305, USA
[8] Institute of Cosmology & Gravitation, University of Portsmouth, Portsmouth, PO1 3FX, UK
[9] Cerro Tololo Inter-American Observatory, National Optical Astronomy Observatory, Casilla 603, La Serena, Chile
[10] Department of Physics & Astronomy, University College London, Gower Street, London, WC1E 6BT, UK
[11] Department of Physics and Electronics, Rhodes University, P.O. Box 94, Grahamstown, 6140, South Africa
[12] Fermi National Accelerator Laboratory, P.O. Box 500, Batavia, IL 60510, USA
[13] CNRS, UMR 7095, Institut d'Astrophysique de Paris, F-75014, Paris, France
[14] Sorbonne Universités, UPMC Univ Paris 06, UMR 7095, Institut d'Astrophysique de Paris, F-75014, Paris, France
[15] Department of Physics and Astronomy, University of Pennsylvania, Philadelphia, PA 19104, USA
[16] Laboratório Interinstitucional de e-Astronomia—LIneA, Rua Gal. José Cristino 77, Rio de Janeiro, RJ-20921-400, Brazil
[17] Observatório Nacional, Rua Gal. José Cristino 77, Rio de Janeiro, RJ-20921-400, Brazil
[18] Department of Astronomy, University of Illinois, 1002 W. Green Street, Urbana, IL 61801, USA
[19] National Center for Supercomputing Applications, 1205 West Clark Street, Urbana, IL 61801, USA
[20] Institut de Ciències de l'Espai, IEEC-CSIC, Campus UAB, Carrer de Can Magrans, s/n, E-08193 Bellaterra, Barcelona, Spain
[21] ARC Centre of Excellence for All-sky Astrophysics (CAASTRO), Australian National University, Canberra, ACT 2611, Australia
[22] The Research School of Astronomy and Astrophysics, Australian National University, ACT 2601, Australia
[23] Astrophysics Research Institute, Liverpool John Moores University, IC2, Liverpool Science Park, Brownlow Hill, Liverpool, L5 3AF, UK
[24] School of Physics and Astronomy, University of Southampton, Southampton, SO17 1BJ, UK
[25] School of Mathematics and Physics, University of Queensland, Brisbane, QLD 4072, Australia
[26] Excellence Cluster Universe, Boltzmannstrasse 2, D-85748 Garching, Germany
[27] Department of Astronomy, University of Michigan, Ann Arbor, MI 48109, USA
[28] Department of Physics, University of Michigan, Ann Arbor, MI 48109, USA
[29] Kavli Institute for Cosmological Physics, University of Chicago, Chicago, IL 60637, USA
[30] Centre for Astrophysics & Supercomputing, Swinburne University of Technology, Victoria 3122, Australia
[31] Department of Astronomy, University of California, Berkeley, 501 Campbell Hall, Berkeley, CA 94720, USA
[32] Lawrence Berkeley National Laboratory, 1 Cyclotron Road, Berkeley, CA 94720, USA
[33] Max Planck Institute for Extraterrestrial Physics, Giessenbachstrasse, D-85748 Garching, Germany
[34] Universitäts-Sternwarte, Fakultät für Physik, Ludwig-Maximilians Universität München, Scheinerstrasse 1, D-81679 München, Germany
[35] Astrophysics & Cosmology Research Unit, School of Mathematics, Statistics & Computer Science, University of KwaZulu-Natal, Westville Campus, Durban 4041, South Africa
[36] Center for Cosmology and Astro-Particle Physics, The Ohio State University, Columbus, OH 43210, USA
[37] Department of Physics, The Ohio State University, Columbus, OH 43210, USA
[38] Jodrell Bank Center for Astrophysics, School of Physics and Astronomy, University of Manchester, Oxford Road, Manchester, M13 9PL, UK
[39] Australian Astronomical Observatory, North Ryde, NSW 2113, Australia
[40] Sydney Institute for Astronomy, School of Physics, A28, The University of Sydney, NSW 2006, Australia
[41] Departamento de Física Matemática, Instituto de Física, Universidade de São Paulo, CP 66318, CEP 05314-970, São Paulo, SP, Brazil
[42] Institute for Astronomy, University of Edinburgh, Royal Observatory, Blackford Hill, Edinburgh, EH9 3HJ, UK
[43] George P. and Cynthia Woods Mitchell Institute for Fundamental Physics and Astronomy, and Department of Physics and Astronomy, Texas A&M University, College Station, TX 77843, USA
[44] Department of Astronomy, The Ohio State University, Columbus, OH 43210, USA
[45] Department of Astrophysical Sciences, Princeton University, Peyton Hall, Princeton, NJ 08544, USA
[46] Institució Catalana de Recerca i Estudis Avançats, E-08010 Barcelona, Spain
[47] Institut de Física d'Altes Energies (IFAE), The Barcelona Institute of Science and Technology, Campus UAB, E-08193 Bellaterra (Barcelona) Spain
[48] Jet Propulsion Laboratory, California Institute of Technology, 4800 Oak Grove Drive, Pasadena, CA 91109, USA
[49] BIPAC, Department of Physics, University of Oxford, Denys Wilkinson Building, 1 Keble Road, Oxford OX1 3RH, UK
[50] Centro de Investigaciones Energéticas, Medioambientales y Tecnológicas (CIEMAT), Madrid, Spain
[51] Instituto de Física, UFRGS, Caixa Postal 15051, Porto Alegre, RS-91501-970, Brazil

[52] Instituto de Astrofísica e Ciências do Espaço, Universidade do Porto, CAUP, Rua das Estrelas, 4150-762 Porto, Portugal
[53] Departamento de Física e Astronomia, Faculdade de Ciências, Universidade do Porto, Rua do Campo Alegre, 687, 4169-007 Porto, Portugal
[54] Argonne National Laboratory, 9700 South Cass Avenue, Lemont, IL 60439, USA

Accepted 2016 February 25

ABSTRACT

We describe updates to the redMaPPer algorithm, a photometric red-sequence cluster finder specifically designed for large photometric surveys. The updated algorithm is applied to 150 deg^2 of Science Verification (SV) data from the Dark Energy Survey (DES), and to the Sloan Digital Sky Survey (SDSS) DR8 photometric data set. The DES SV catalog is locally volume limited and contains 786 clusters with richness $\lambda > 20$ (roughly equivalent to $M_{500c} \gtrsim 10^{14}\, h_{70}^{-1}\, M_\odot$) and $0.2 < z < 0.9$. The DR8 catalog consists of 26,311 clusters with $0.08 < z < 0.6$, with a sharply increasing richness threshold as a function of redshift for $z \gtrsim 0.35$. The photometric redshift performance of both catalogs is shown to be excellent, with photometric redshift uncertainties controlled at the $\sigma_z/(1+z) \sim 0.01$ level for $z \lesssim 0.7$, rising to $\sim$0.02 at $z \sim 0.9$ in DES SV. We make use of *Chandra* and *XMM* X-ray and South Pole Telescope Sunyaev–Zeldovich data to show that the centering performance and mass–richness scatter are consistent with expectations based on prior runs of redMaPPer on SDSS data. We also show how the redMaPPer photo-z and richness estimates are relatively insensitive to imperfect star/galaxy separation and small-scale star masks.

Key words: galaxies: clusters: general

Supporting material: FITS files

1. INTRODUCTION

Clusters of galaxies are the largest bound objects in the universe and are uniquely powerful cosmological probes (e.g., Henry et al. 2009; Vikhlinin et al. 2009; Mantz et al. 2010; Rozo et al. 2010; Clerc et al. 2012; Benson et al. 2013; Hasselfield et al. 2013; Planck Collaboration et al. 2014; see also reviews in Allen et al. 2011; Weinberg et al. 2013). In particular, galaxy clusters are one of the key probes of the growth of structure and dark energy measurements from ongoing and upcoming photometric surveys such as the Dark Energy Survey (DES; The DES Collaboration 2005), the Kilo-Degree Survey (KiDS; de Jong et al. 2015), the Hyper-Suprime Camera (HSC),[55] the Large Synoptic Survey Telescope (LSST; LSST Science Collaboration et al. 2009), *Euclid* (Laureijs et al. 2011), and WFIRST.[56]

A wide range of photometric cluster finders already exists (e.g., Goto et al. 2002; Gladders et al. 2007; Koester et al. 2007a; Hao et al. 2010; Soares-Santos et al. 2011; Szabo et al. 2011; Ascaso et al. 2012, 2014; Murphy et al. 2012; Wen et al. 2012; Oguri 2014), each with various strengths and weaknesses. In 2014, we introduced the red-sequence matched-filter Probabalistic Percolation cluster finder (redMaPPer; Rykoff et al. 2014, henceforth RM1). RedMaPPer identified galaxy clusters by making use of the fact that the bulk of the cluster population is made up of old, red galaxies with a prominent 4000 Å break. Focusing on this specific galaxy population increases the contrast between cluster and background galaxies in color space, and enables accurate and precise photometric redshift (photo-z) estimates. The associated cluster richness estimator, λ, is the sum of of the membership probability of every galaxy in the cluster field and has been optimized to reduce the scatter in the richness–mass relation (Rozo et al. 2009, 2011; Rykoff et al. 2012).

The initial application of redMaPPer in RM1 was to the Sloan Digital Sky Survey Data Release 8 photometric data (SDSS DR8; York et al. 2000; Aihara et al. 2011). As such, the catalog was limited to relatively low redshifts ($z \lesssim 0.5$). The SDSS redMaPPer catalog has been extensively validated using X-ray (Rozo & Rykoff 2014, henceforth RM2; Sadibekova et al. 2014) and Sunyaev–Zeldovich (SZ) data (Rozo et al. 2015a, henceforth RM3), and with spectroscopic data (Rozo et al. 2015b, henceforth RM4), demonstrating that the catalog has low scatter in its mass–richness relation, well-quantified centering performance, and accurate and precise cluster photo-zs. The low scatter has also made it possible to use the redMaPPer SDSS catalog to verify Planck clusters (Planck Collaboration et al. 2015; Rozo et al. 2015a). In a comparison of numerous spectroscopic cluster finders on mock catalogs, redMaPPer achieved one of the smallest variances in estimated cluster mass at fixed halo mass, despite being the only cluster finder relying solely on two-band photometric data (all of the other cluster finders were spectroscopic; Old et al. 2015).

RedMaPPer was designed to easily handle a broad range in redshift, as well as to run efficiently over a wide and deep galaxy catalog. As such, it is ideally suited to DES data, which can be used to detect faint, red-sequence galaxies to much higher redshifts than SDSS ($z \lesssim 0.9$). In this paper, we describe the first application of redMaPPer to DES Science Verification (SV) data. In addition, we describe updates to the redMaPPer algorithm since versions 5.2 (RM1) and 5.10 (RM4) to the present version 6.3, and apply the updated algorithm to the SDSS DR8 photometric data. We characterize the photo-z performance of redMaPPer using available spectroscopy, and use available SZ data from the South Pole Telescope SZ cluster survey (SPT; Bleem et al. 2015), as well as X-ray observations from *Chandra* and *XMM*, to measure the centering properties of the DES SV redMaPPer catalog and to test the validity of the redMaPPer cluster richness as a photometric mass tracer. A detailed analysis of the richness and SZ scaling relations is presented in Saro et al. (2015, henceforth S15). A similar analysis of X-ray observations including SDSS overlap will be presented in A. Bermeo Hernendez et al. (2016, in preparation) and D. Hollowood et al. (2016, in preparation).

[55] http://www.naoj.org/Projects/HSC/HSCProject.html
[56] http://wfirst.gsfc.nasa.gov/

The layout of this paper is as follows. In Section 2 we describe the DES SV and SDSS DR8 data used in this work. Section 3 describes the updates to the redMaPPer algorithm since the RM1 and RM4 papers. Section 4 describes the cluster catalogs, as well as the photometric redshift performance on DES and SDSS data. In Section 5, we detail the effects of star/galaxy separation and small-scale masking on the cluster properties, and in Section 6 we compare the redMaPPer catalog with X-ray and SZ clusters in the DES SVA1 footprint. Finally, in Section 7, we summarize our results. When necessary, distances are estimated assuming a flat ΛCDM model with $\Omega_m = 0.30$. For consistency with previous redMaPPer work, we use $h = 1.0$ when quoting distances (h^{-1} Mpc) and $h = 0.7$ when quoting masses ($h_{70}^{-1} M_\odot$).

2. DATA

2.1. DES SV Data

DES is an ongoing five-band (*grizY*) photometric survey performed with the Dark Energy Camera (DECam, Flaugher et al. 2015) on the 4 m Blanco Telescope at Cerro Tololo Inter-American Observatory (CTIO). Prior to the beginning of the DES, from 2012 November to 2013 March, DES conducted a ∼250 deg^2 "SV" survey. The largest contiguous region covers ∼160 deg^2 of the eastern edge of the SPT survey ("SPT-E" hereafter). A smaller ∼35 deg^2 region is in the western edge of the footprint ("SPT-W" hereafter). In addition, the DES surveys 10 Supernova fields ("SN fields" hereafter) every 5–7 days, each of which covers a single DECam 2.2-degree-wide field of view, for a total of ∼32 deg^2 of deeper imaging (including extra offset pointings of SN fields taken during SV). Finally, there are smaller discontinuous regions targeting massive clusters (Melchior et al. 2015) and the COSMOS field (Scoville et al. 2007). We utilize this DES SV data set to construct the first DES redMaPPer cluster catalog. The redMaPPer footprint used in this paper is the same as that used for the associated redMaGiC (red-sequence matched-filter Galaxies Catalog) of red galaxies with well-behaved photo-z performance (Rozo et al. 2015c, henceforth RM15).

The DES SV data were processed by the DES Data Management (DESDM) infrastructure (R. Gruendl et al 2016, in preparation), which includes image detrending, astrometric registration, global calibration, image coaddition, and object catalog creation. Details of the DES single-epoch and coadd processing can be found in Sevilla et al. (2011) and Desai et al. (2012). We use `SExtractor` to create object catalogs from the single-epoch and coadded images (Bertin & Arnouts 1996; Bertin 2011).

After the initial production of these early data products, we detected several issues that were mitigated in post-processing, leading to the creation of the "SVA1 Gold" photometry catalog.[57] First, we masked previously unmasked satellite trails. Second, we use a modified version of the `big-macs` stellar-locus regression (SLR) fitting code (Kelly et al. 2014)[58] to recompute coadded zero-points over the full SVA1 footprint. Third, regions around bright stars ($J < 13$) from the Two Micron All Sky Survey (2MASS; Skrutskie et al. 2006) were masked. Finally, we removed 4% of the area with a large concentration of centroid shifts between bandpasses in individual objects, indicating scattered light, ghosts, satellite trails, and other artifacts (Jarvis et al. 2015, Section 2.1). We utilize the `SExtractor MAG_AUTO` quantity derived from the coadded images for galaxy total magnitudes and colors. This choices reflects the fact that methods used to compute multi-epoch fitting photometric quantities are still under development. The added noise in the color results in a larger observed red-sequence width, which results in slightly poorer photometric redshifts, as shown in Section 4.1.2. For the present work, we have not made use of the DES *Y*-band imaging because of uncertain calibration and the minimal lever-arm gained at the redshifts probed in this paper. Finally, our fiducial star/galaxy separation is performed with the multi-band multi-epoch image processing code `ngmix` used for galaxy shape measurement in DES data (Jarvis et al. 2015), as detailed in Appendix A of RM15.

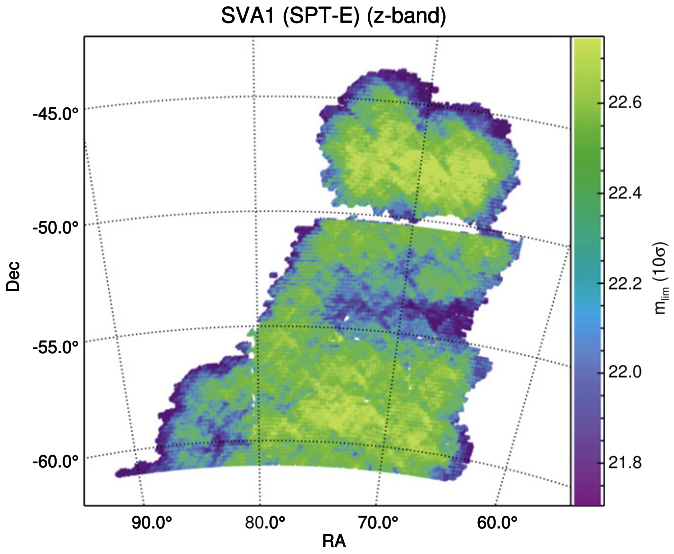

Figure 1. Map of 10σ depth (in magnitudes) in ∼125 deg^2 in the SVA1 SPT-E footprint for SLR-corrected $z_{\rm auto}$ magnitudes. Small-scale variations are caused by variations in the number of exposures, chip gaps, and observing conditions.

The footprint is initially defined by `MANGLE` (Swanson et al. 2008) maps generated by DESDM which describe the geometry of the coadded data in polygons of arbitrary resolution. For ease of use, these are then averaged over `HEALPIX NSIDE=4096` pixels (Górski et al. 2005), where each pixel is approximately 0.′7 on a side. The pixelized `MANGLE` maps are combined with maps of the survey observing properties (e.g., airmass, FWHM, etc.) compiled by Leistedt et al. (2015) using the method of Rykoff et al. (2015) to generate 10σ `MAG_AUTO` limiting magnitude maps. We first restrict the footprint to regions with deep `MAG_AUTO` in the z band ($m_{z,\rm lim}$) such that $m_{z,\rm lim} > 22$, as shown in Figure 1 for ∼125 deg^2 in the SPT-E region.[59] Only galaxies brighter than the local 10σ limiting magnitude are used in the input catalog.

The `ngmix` runs used for star/galaxy separation in this paper and in RM15 were primarily used for galaxy shape estimation for DES cosmic shear (Becker et al. 2015) and cosmological constraints (The Dark Energy Survey Collaboration et al. 2015). Therefore, the runs were performed on regions with very tight tolerance for image quality and were restricted

[57] http://des.ncsa.illinois.edu/releases/sva1

[58] https://code.google.com/p/big-macs-calibrate/

[59] This is equivalent to a $0.2L^*$ galaxy at $z = 0.65$, as described in Section 3.2.

to the largest contiguous region (SPT-E) as well as to supplementary runs on the SN fields. These regions comprise our fiducial footprint for the input galaxy catalog of 148 deg^2 (of which 125 deg^2 is in SPT-E). However, mask boundaries and holes reduce the effective area for extended cluster sources to $\sim$100 deg^2 (see Section 3.6 for details). In Section 5, we describe an expanded footprint where we relax some of these constraints, and include SPT-W and COSMOS, with less robust star/galaxy separation.

The spectroscopic data used in this paper comes from the Galaxy and Mass Assembly survey (GAMA Driver et al. 2011), the VIMOS VLT Deep Survey (VVDS Garilli et al. 2008), the 2dF Galaxy Redshift Survey (2dFGRS Colless et al. 2001), SDSS (Ahn et al. 2013), the VIMOS Public Extragalactic Survey (VIMOS Garilli et al. 2014), and the Arizona CDFS Environment Survey (ACES Cooper et al. 2012). In addition, we have a small sample of cluster redshifts from SPT used in the cluster validation of Bleem et al. (2015). These data sets have been further supplemented by galaxy spectra acquired as part of the OzDES spectroscopic survey, which is performing spectroscopic follow-up on the AAOmega instrument at the Anglo-Australian Telescope in the DES supernova fields (Yuan et al. 2015). In all, there are 36,607 photometric galaxies with spectroscopic redshifts in our input catalog, although only $\sim$2000 are red cluster members, and $\sim$1400 are used in the calibration of the red sequence in Section 3.3.

2.2. SDSS DR8

In addition to our new catalog of DES SVA1 data, we have updated the redMaPPer catalog for SDSS DR8 photometric data (Aihara et al. 2011), which remains the most recent photometric data release from SDSS. The DR8 galaxy catalog contains $\sim$14,000 deg^2 of imaging, which we cut to the 10,401 deg^2 of contiguous high-quality observations using the mask from the Baryon Acoustic Oscillation Survey (BOSS, Dawson et al. 2013). The mask is further extended to exclude all of the stars in the Yale Bright Star Catalog (Hoffleit & Jaschek 1991), as well as the area around objects in the New General Catalog (Sinnott 1988). The resulting mask is that used by RM1 to generate the SDSS DR8 redMaPPer catalog. We refer the reader to that work for further discussion on the mask, as well as object and flag selection.

Total magnitudes are determined from *i*-band SDSS `CMODEL_MAG`, which we denote as m_i, and colors from *ugriz* SDSS `MODEL_MAG`. All of our spectroscopy is drawn from SDSS DR10 (Ahn et al. 2013). Finally, we make use of the 10σ limiting magnitude maps from Rykoff et al. (2015, see, e.g., Figure 4). As with SVA1 data, only galaxies brighter than the local 10σ limiting magnitude are used in the input catalog.

3. UPDATES TO THE REDMAPPER ALGORITHM

RedMaPPer is a matched-filter, red-sequence photometric cluster finding algorithm with three filters based on galaxy color, position, and luminosity. The most important filter characterizes the color of red-sequence galaxies as a function of redshift. This filter is a linear red-sequence model in color–magnitude space (with slope and intercept) in $n_{\rm col}$ dimensions, where $n_{\rm col}$ is the number of independent colors in the input data set. The filter also incorporates the intrinsic scatter, $C_{\rm int}$, which is the $n_{\rm col} \times n_{\rm col}$ covariance matrix assuming Gaussian errors in photometric magnitudes. This filter is self-calibrated by making use of clusters with known spectroscopic redshifts. The two additional filters are the radial filter, comprised of a projected Navarro–Frenk–White profile (Navarro et al. 1994), and a luminosity filter based on a Schechter function. Once the parameters of the red-sequence filter are known, we use this information to compute the probability $p_{\rm mem}$ that each galaxy in the vicinity of the cluster is a red-sequence member. The richness λ is defined as the sum of the membership probabilities over all of the galaxies within a scale-radius R_λ:

$$\lambda = \sum p_{\rm mem}\, \theta_L\, \theta_R, \tag{1}$$

where θ_L and θ_R are the luminosity- and radius-dependent weights defined in Appendix B of RM4. The radius scales with the size of the cluster such that $R_\lambda = 1.0(\lambda/100)^{0.2} h^{-1}$ Mpc, which we have shown minimizes the scatter in the mass–richness relation (Rykoff et al. 2012). All of the galaxies with magnitudes consistent with being brighter than $0.2\,L_*$ are considered for computing the richness, as described below in Section 3.2. We note that the weights θ_L and θ_R are "soft cuts" to ensure that cluster richness measurements are robust to small perturbations in galaxy magnitudes. The cluster photometric redshift, z_λ, is constrained at the same time as the cluster richness by fitting all of the possible member galaxies simultaneously to the red-sequence color function.

The above equation describes the richness computation in the absence of any masking (star holes and survey boundaries), and in the regime where the local limiting magnitude is deeper than $0.2\,L_*$ at the cluster redshift. As described in Section 5 of RM1, we additionally compute a scale factor S to correct for these missing cluster members, such that

$$\frac{\lambda}{S} = \sum_{\rm gals} p_{\rm mem}, \tag{2}$$

so that each cluster with richness λ has λ/S galaxies brighter than the limiting magnitude of the survey within the geometric survey mask. At the same time, we estimate the variance S which is used in the computation of the uncertainty on richness λ, as detailed in Appendix B of RM4. In this way, the total uncertainty on λ includes the uncertainty from correcting for mask and depth effects.

In addition, as described in Section 5.1 of RM1 (specifically Equation (24)), it is useful to compute the fraction of the effective cluster area that is masked solely by geometric factors such as stars, bad regions, and survey edges. This mask fraction, denoted $f_{\rm mask}$, is complementary to S above in that it contains all of the local masking except the depth limit.

In addition to estimating membership probabilities, the redMaPPer centering algorithm is also probabilistic (see Section 8 of RM1). The centering probability $P_{\rm cen}$ is a likelihood-based estimate of the probability that a galaxy under consideration is a central galaxy (CG). This likelihood includes the fact that the photo-z of the CG must be consistent with the cluster redshift, that the CG luminosity must be consistent (using a Gaussian filter) with the expected luminosity of the CG of a cluster of the observed richness, and that the local red galaxy density (on the scale of $\sim$200 h^{-1} kpc) is consistent with that of CGs. We additionally assume that each cluster can have at most one CG, and store the top 5 most likely central candidates. Our fiducial cluster position is given by the highest

likelihood central galaxy. Because of the luminosity filter, the CG candidate with the largest $P_{\rm cen}$ tends to be very bright, but is not necessarily the brightest member. Thus, we do not refer to it as the brightest cluster galaxy, only as the CG. Typically, for ~15%–20% of the clusters, the CG chosen by redMaPPer is not the brightest member.

The redMaPPer algorithm has previously been applied to SDSS DR8 photometric data. For more details on the redMaPPer algorithm, we refer the reader to RM1 and the updates in the appendix of RM4. In this section, we detail the various modifications that have been implemented on the redMaPPer algorithm since its last public data release (RM4).

3.1. Incorporating Small-scale Structure in the Local Survey Depth

Variable survey depth can lead to galaxies being "masked out" from galaxy clusters. Specifically, if a member galaxy (with $L \geqslant 0.2L_*$) has a magnitude below our brightness threshold, then one needs to statistically account for this missing galaxy, as per the above formalism. To do so, however, one needs to know the survey depth over the full area coverage of the galaxy cluster.

The original redMaPPer application to SDSS DR8 in RM1 (redMaPPer v5.2) assumed that the survey had a uniform depth with $m_i < 21.0$. In the update described in RM4 (redMaPPer v5.10), we empirically computed the local survey depth averaged over the location of each cluster. This was superior to assuming a constant-depth survey, but ignored small-scale depth variations, as well as being somewhat noisy. In this updated version (redMaPPer v6.3), we have extended redMaPPer to incorporate variable survey limiting magnitude maps as detailed in Rykoff et al. (2015) and described in Section 2. Specifically, we utilize the local survey depth from these depth maps to estimate the fraction of cluster galaxies that are masked, as defined in Section 3 and detailed in Appendix B of RM4. In the present version of the algorithm, we assume that the red galaxy detection is complete (modulo masking) at magnitudes brighter than the local 10σ limiting magnitude used to select the input catalog. In future versions, we intend to track the full completeness function, as described in Section 5 of Rykoff et al. (2015).

3.2. Generalization of the Characteristic Magnitude $m_*(z)$ to Arbitrary Survey Filters

As with the previous versions of the redMaPPer algorithm, our luminosity filter is based on a Schechter function (e.g., Hansen et al. 2009) of the form

$$\phi(m_i) \propto 10^{-0.4(m_i-m_*)(\alpha+1)}\exp(-10^{-0.4(m_i-m_*)}), \qquad (3)$$

where we set the faint-end slope $\alpha = 1.0$ independent of redshift. Previously, we set the characteristic magnitude, $m_*(z)$, using a k-corrected, passively evolving stellar population which we had derived from a PEGASE.2 stellar population/galaxy formation model (Fioc & Rocca-Volmerange 1997; Eisenstein et al. 2001; Koester et al. 2007b). As this was derived specifically for the SDSS filters at relatively low redshift, we have updated our reference $m_*(z)$ to more simply allow for different filter sets and a broader redshift range.

The new value of $m_*(z)$ is computed using a Bruzual & Charlot (2003, BC03) model to predict the magnitude evolution of a galaxy with a single star formation burst at $z = 3$ (with solar metallicity and Salpeter IMF) as implemented in the `EzGal` Python package (Mancone & Gonzalez 2012). We normalize m_* so that $m_{i,\rm SDSS} = 17.85$ at $z = 0.2$ for an L_* galaxy. This was chosen to match the $m_*(z)$ relation from RM1 and Rykoff et al. (2012). We have additionally confirmed that the evolution of $m_*(z)$ is within 8% of that used in RM1 over the RM1 redshift domain ($0.1 < z < 0.5$), with the largest deviations at $z \sim 0.5$. The normalization condition for m_z for DES is then derived from the BC03 model using the DECam passbands (Flaugher et al. 2015).

3.3. Initial Selection of Red Spectroscopic Galaxies

As described in RM1, the initial calibration of the red sequence relies on spectroscopic "seed" galaxies. This may be comprised of a set of training clusters with spectroscopic redshifts (as in DES SVA1) or a large spectroscopic catalog with a sufficient number of red galaxies in clusters (as in SDSS DR8). In RM1 (see Section 6.2), we selected red galaxies by splitting the spectroscopic catalog into narrow redshift bins and using a Gaussian mixture model (Hao et al. 2009) to separate galaxies in each redshift bin into blue and red components. However, we have found that this method is only robust when we have a plethora of spectra, as is the case with SDSS.

In this paper, the initial red galaxy selection is performed by computing the color residuals of galaxies in a broad range of redshifts relative to the BC03-derived color models from Section 3.2. As we are only concerned with making an initial selection of red and blue galaxies, any color calibration offsets between the data and the BC03 model are irrelevant; we just need to get an initial sample of red galaxies. We again employ a Gaussian mixture model to obtain a first estimate for the mean color and intrinsic scatter of the red spectroscopic galaxies. To ensure a clean selection, we use the $g - r$ color for $z_{\rm spec} < 0.35$; $r - i$ for $0.35 < z_{\rm spec} < 0.7$; and $i - z$ for $z_{\rm spec} > 0.7$. At this point, we proceed as described in Step 3 of RM1, Section 6.2.

3.4. Redshift Reach of the Cluster Catalog

Ideally, a photometric survey would be deep enough to detect the faintest $0.2L_*$ galaxies that contribute to our richness estimator λ over the full redshift range and footprint of the catalog. In a roughly uniform survey such as the SDSS, this limitation translates into a maximum redshift, $z_{\rm max}$, below which the cluster catalog is volume limited; for SDSS, $z_{\rm max} < 0.33$. By contrast, the observing strategy of a multi-epoch survey such as the DES may yield much greater depth variations, as shown in Figure 1. Furthermore, the depth variations can be different in different bands. Consequently, the redshift range that can be successfully probed with redMaPPer will depend on the local survey depth, with deeper regions allowing us to detect galaxy clusters to higher redshifts.

We define a maximum redshift $z_{\rm max}$ at each position in the sky as follows. Given a point in the survey, our initial depth map for the main detection band (m_z in the case of SVA1), and a luminosity threshold ($L_{\rm thresh}$), we calculate the maximum redshift to which a typical red galaxy (defined by our red-sequence model) of $L_{\rm thresh}$ is detectable at $>10\sigma$ in the main detection band (z band for DES), and at $>5\sigma$ in the remaining bands. Only clusters with $z \leqslant z_{\rm max}$ are accepted into our cluster catalog, with $z_{\rm max}$ defining the redshift component of our survey mask. In this way, we can simply (and conservatively)

account for the regions that are extremely shallow in one or more bands. This happens in SVA1 primarily at the boundaries, and other regions that were observed in non-photometric conditions. The result is a map of $z_{\rm max}$ in HEALPIX format with NSIDE=4096, where each pixel is approximately 0.′7 on a side, which is matched to the resolution of the input depth maps.

Given this procedure, we still have an arbitrary decision as to where to set our luminosity threshold $L_{\rm thresh}$. The most conservative option would be to demand that every cluster in the final catalog be at a redshift such that we can detect red galaxies to $L_{\rm thresh} = 0.2L_*$. However, we have chosen to be somewhat more aggressive in the interest of increasing the number of galaxy clusters and redshift reach of the DES SV catalog, as the impact on the uncertainty estimate of λ (see Equation (2)) is modest for clusters that only require a small extrapolation. For SVA1, we have chosen the luminosity threshold to be $L_{\rm thresh} = 0.4L_*$ for the construction of the $z_{\rm max}$ map. For DR8, we have chosen $L_{\rm thresh} = 1.0L_*$, such that $z_{\rm max} \sim 0.6$ over >99% of the DR8 footprint. Although this requires a large richness extrapolation at high redshift (and hence large richness errors), this cut maintains consistency with previous redMaPPer catalogs (versions 5.2 and 5.10) where we did not use a $z_{\rm max}$ map. However, if users wish to utilize a volume-limited subset of the DR8 redMaPPer catalog, a restriction of $z_\lambda < 0.33$ will ensure that the local depth at every cluster is deep enough to detect $0.2L_*$ galaxies.

3.5. Differences Between the SVA1 and DR8 Analyses

Although the code used to run on SVA1 and DR8 is the same, there are a few key differences that we highlight here.

1. For DR8, we use the *i* band for the detection magnitude; for SVA1, we use the z band, which is better suited to the broad redshift range and the excellent *z*-band performance of DECam.
2. For DR8, we use *ugriz* for galaxy colors, while for SVA1 we only use *griz*. The lack of a *u* band has a negligible effect on the cluster detection and cluster photo-*z*s at $z > 0.2$ (see Section 8.1 of RM15).
3. For DR8, reddening corrections are applied to catalog magnitudes. For SVA1, these are incorporated into the SLR zero-point calibration.
4. For DR8, we train the red-sequence model over 2000 deg^2 (∼20% of the full footprint), as in RM1, to ensure sufficient statistics of spectroscopic training while avoiding any possibility of over-training. For the much smaller SVA1 catalog, we use the full footprint and all available spectra. The impact of this is detailed in Section 4.1.2.

3.6. Generation of Random Points

In RM1, we describe a method of estimating the purity and completeness of the cluster catalog using the data itself, by placing fake clusters into the data and recovering the richness. While this method (described in Section 11 of RM1) is useful for estimating the selection function and projection effects, it is not appropriate for generating a cluster random catalog for cross-correlation measurements, such as the cluster–shear cross-correlation used for stacked weak-lensing mass estimates (e.g., Johnston et al. 2007; Reyes et al. 2008), as existing large-scale structure is imprinted on the random catalog.

In this section, we describe a new way of generating cluster random points by making use of the $z_{\rm max}$ map from Section 3.4. A particular challenge is the fact that galaxy clusters are extended objects, and thus the detectability depends not just on the redshift, but also on the cluster size and the survey boundaries. We generate a random cluster catalog that has the same richness and redshift distribution of the data catalog by randomly sampling $\{\lambda, z_\lambda\}$ pairs from the data catalog. To ensure that the random catalog correctly samples the survey volume, we utilize the redshift mask. Specifically, after sampling a cluster from the cluster catalog, we randomly sample a position ($\{\alpha, \delta\}$) for the random point. If the cluster redshift z_λ is larger than the maximum redshift at which the cluster can be detected, then we draw a new $\{\alpha, \delta\}$, repeating the procedure until the cluster is assigned a position consistent with the cluster properties. In all, we sample each cluster $n_{\rm samp} \sim 1000$ times to ensure that any correlation measurements we make are not affected by noise in the random catalog.

Having assigned a position, we use the depth map and the footprint mask to estimate the local mask fraction $f_{\rm mask}$ and scale factor *S*, as defined in Section 3. This is the point at which the finite extent of the clusters is taken into account. Only random points that have $f_{\rm mask} < 0.2$ and $\lambda/S > 20$ are properly within the cluster detection footprint. These cuts will locally modify the richness and redshift distribution of the random points relative to the data. In particular, the random points will tend to undersample the regions from which we discard clusters, particularly for low-richness and high-redshift clusters.

We address this difficulty by using weighted randoms. Specifically, given all of the $n_{\rm samp}$ random points generated from a given $\{\lambda, z_\lambda\}$ pair, we calculate the number of random points that pass our mask and threshold cuts, denoted as $n_{\rm keep}$. Each random point is then upweighted by a factor $w = n_{\rm samp}/n_{\rm keep}$. This ensures that the weighted distribution of random points matches the cluster catalog as a function of both λ and z_λ, while taking into account all of the boundaries and depth variations. As we typically sample each cluster ∼1000 times, the weight *w* is sufficiently well measured that we neglect noise in *w* when making use of the weighted random points. We note that in this procedure, we neglect sample variance from large-scale structure that may be imprinted in the cluster catalog; while this may be a small issue for SVA1, this will be averaged out over large surveys such as DES and SDSS.

Finally, we compute the effective area of the survey for cluster detection. For any given redshift *z*, we compute the total area ($A_{\rm tot}$) covered where we might have a chance of detecting a cluster, such that $z < z_{\rm max}$. Taking into account boundaries and the finite size of clusters, the effective area is simply $A_{\rm tot} \times n_{\rm samp}/n_{\rm keep}$, where $n_{\rm samp}/n_{\rm keep}$ is computed for all random points with $z < z_{\rm max}$. We then use a cubic spline to perform a smooth interpolation as a function of redshift. Due to the finite size of the clusters and the small footprint of SVA1 with a lot of boundaries, the effective area for $\lambda > 20$ cluster detection is reduced from 148 deg^2 to ∼100 deg^2 at $z < 0.6$.

4. THE FIDUCIAL CLUSTER CATALOGS

We have run the updated redMaPPer v6.3 algorithm on SDSS DR8 and DES SVA1 data as described in Section 2.

Table 1

redMaPPer Cluster Samples

Sample	Area (deg^2)[a]	Redshift Range	No. of Clusters[b]
DR8	10134	$0.08 < z_\lambda < 0.6$	26111
SVA1	116	$0.2 < z_\lambda < 0.9$	787
SVA1 expanded	208	$0.2 < z_\lambda < 0.9$	1382

Notes.
[a] Area including the effect of the $f_{\rm mask} < 0.2$ cut for extended cluster sources (see Section 3.6).
[b] Richness threshold, $\lambda/S > 20$.

Following RM1, the full cluster finder run contains all of those clusters with $\lambda \geqslant 5\,S$ over the redshift ranges $z_\lambda \in [0.05, 0.6]$ (for DR8) and $z_\lambda \in [0.15, 0.9]$ (for SVA1). However, we have chosen to apply relatively conservative cuts to our catalogs. The cuts we apply are as follows.

1. There must be at least 20 unmasked galaxies brighter than the local limiting magnitude, such that $\lambda/S > 20$.
2. The volume-limited mask for SVA1 is as described above. The volume-limited catalog for DR8 is simply $z_\lambda < 0.33$.
3. For the DR8 catalog, the richness scale factor $S(z)$ is illustrated by Figure 19 in RM1. For the volume-limited SVA1 catalog, $S(z) \lesssim 1.3$ at all redshifts by construction.
4. Very low-redshift clusters have biased redshifts and richnesses due to boundary effects, and so we have set the lower-redshift limit at $z_\lambda > 0.08$ and $z_\lambda > 0.2$ for the DR8 and SVA1 catalogs, respectively.
5. Only clusters with $f_{\rm mask} < 0.2$ are included. That is, clusters near the boundary and on top of masked regions will be removed. The cluster random points properly sample the footprint, reflecting these cuts.

A summary of the number of clusters, effective area, and redshift range of the catalogs (including the SVA1 expanded catalog described in Section 5.2) is given in Table 1.

Figure 2 shows the angular density contrast of our redMaPPer sample for SDSS DR8 ($0.1 < z_\lambda < 0.3$) and Figure 3 shows the same for DES SVA1 ($0.2 < z_\lambda < 0.8$). We restrict ourselves to $z_\lambda < 0.8$ because only the deepest regions (and SN fields) have redMaPPer-selected clusters at $z_\lambda > 0.8$. Due to the relatively small density of clusters on the sky, the density contrast is smoothed on a 30′ scale to suppress noise. Large-scale structure is readily apparent in the cluster density. Previous DES work has shown that the density field of redMaPPer clusters is well correlated with the underlying matter density field as determined from weak-lensing measurements (Chang et al. 2015b; Vikram et al. 2015).

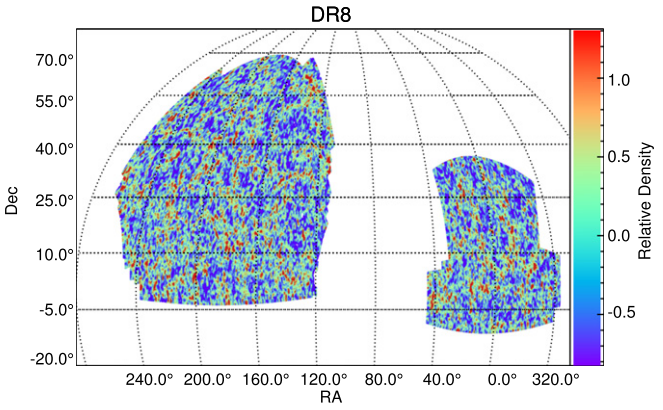

Figure 2. Angular cluster density contrast $\delta = (\rho - \bar{\rho})/\bar{\rho}$ for the SDSS DR8 redMaPPer catalog in the redshift range [0.1, 0.3], averaged on a 30′ scale.

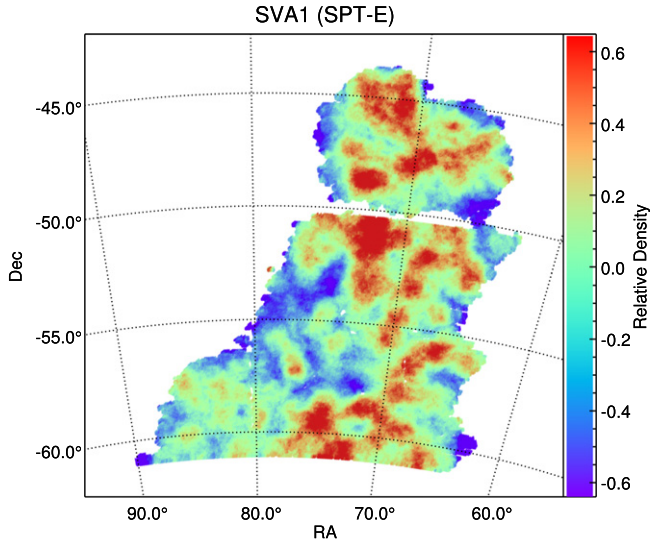

Figure 3. Angular cluster density contrast $\delta = (\rho - \bar{\rho})/\bar{\rho}$ for the DES SVA1 redMaPPer catalog in the redshift range [0.2, 0.8], averaged on a 30′ scale.

4.1. Photo-z Performance

4.1.1. SDSS DR8

In Figure 4, we compare the photometric redshift z_λ to the spectroscopic redshift of the CG (where available) for all of the clusters in DR8 with $\lambda > 20$. The top panel shows a density map of the $z_{\rm spec}$–z_λ relation with 4σ outliers (such that $|(z_{\rm spec}-z_\lambda)/\sigma_{z_\lambda}| > 4$), which make up 1.1% of the population, marked as red points. The outlier clump at $z_\lambda \sim 0.4$ is due to cluster miscentering rather than photometric redshift failures. In RM1, we demonstrated that this clump of outliers is due to errors in cluster centering rather than photometric redshift estimation. Specifically, these outliers represent those clusters in which the photometrically assigned CG has a spectroscopic redshift that is inconsistent not only with the photometric redshift of the cluster, but also with the spectroscopic redshift of the remaining cluster members (see Figure 10 in RM1). This failure mode is particularly pronounced near filter transitions. The bottom panel shows the bias (magenta dotted–dashed line) and scatter (cyan dot–dot–dashed line) about the 1–1 line (blue dashes). The performance is equivalent to that from RM1, with $\sigma_z/(1+z) < 0.01$ over most of the redshift range.

4.1.2. DES SVA1

Figure 5 is the analog to Figure 4 for DES SVA1. Because of the significantly smaller number of spectra, we show all clusters with $\lambda > 5$, despite the fact that this will increase the rate of 4σ outliers due to miscentering. Nevertheless, the performance is still very good with only 5% outliers. All of these outliers have $\lambda < 20$; thus, there are no 4σ outliers in the set of 52 clusters with spectra in the fiducial $\lambda/S > 20$ catalog. The bias and scatter are all very good at $z \lesssim 0.7$, with an increase of $\sigma_z/(1+z)$ from ∼0.01 to ∼0.02 at high redshift. This increase is caused by both the variations in survey depth,

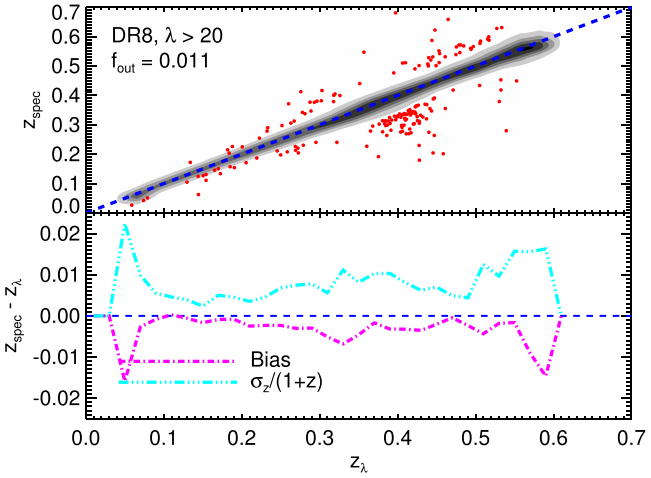

Figure 4. Top: central galaxy spectroscopic redshift $z_{\rm spec}$ vs. cluster photometric redshift z_λ for SDSS DR8 clusters with $\lambda > 20$. Gray shaded regions show 1, 2, and 3σ density contours. Red points, comprising 1.1% of the total sample, show $>4\sigma$ outliers. The outlier clump at $z_\lambda \sim 0.4$ is not due to photometric redshift failures, but rather centering failures: these are primarily clusters with a correct photometric redshift, but whose photometrically assigned central galaxy is not in fact a cluster member. Bottom: bias in $z_{\rm spec} - z_\lambda$ (magenta) and z_λ scatter $\sigma_z/(1+z)$ (cyan) for clusters with central galaxy spectra. Over most of the redshift range, the bias is <0.005 and the scatter $\sigma_z/(1+z) < 0.01$.

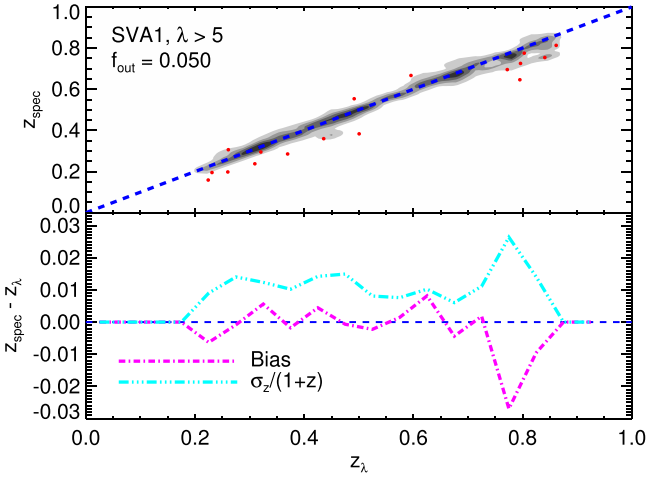

Figure 5. Same as Figure 4, for SVA1 clusters with $\lambda > 5$. The lower richness threshold was used for the plot because of the small number of cluster spectra for $\lambda > 20$ clusters. At $z \gtrsim 0.7$ the scatter increases to $\sigma_z/(1+z) \sim 0.02$ as our red-sequence model is noisy due to the relative lack of training spectra. As discussed in the text, the increased z_λ scatter over all redshifts (relative to DR8) is caused by relatively noisy MAG_AUTO colors.

as well as noise in the high-z red-sequence model that will be reduced as we obtain more cluster spectra and increase our footprint in full DES operations. At low redshift, we note that the scatter in z_λ is larger in DES SVA1 than in SDSS DR8. This is primarily caused by the relatively noisy MAG_AUTO galaxy colors employed for our SVA1 catalog which increase the red-sequence width, and hence the noise, in z_λ.

Because our analysis utilized all of the available spectroscopy for training redMaPPer, it is possible that our photo-z performance is artificially good due to over-training. To test for this, we have performed a second full training of the red-sequence model using only 50% of the cluster spectra, and reserving the second half for a validation test. This is not ideal,

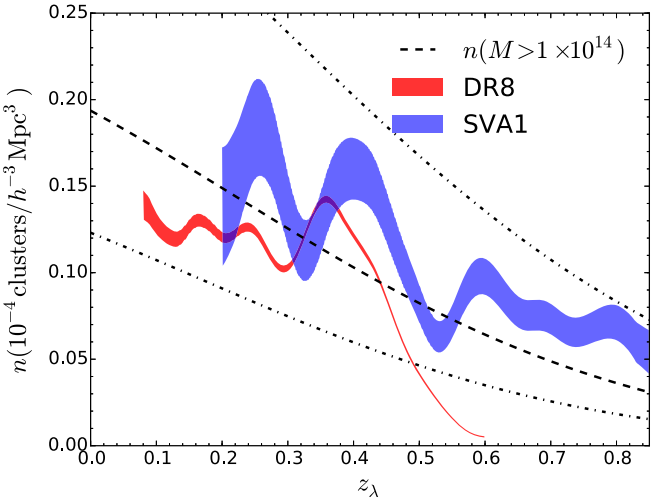

Figure 6. Comoving density of clusters ($\lambda/S > 20$) for DR8 (red curve) and SVA1 (blue curve), assuming our fiducial cosmology. The widths of the lines correspond to the assumption of Poisson errors (which are consistent with jackknife errors). The black dashed line shows the predicted abundance of halos with $M_{500c} > 1 \times 10^{14}\, h_{70}^{-1}\, M_\odot$, with the dash–dotted lines showing the same with a mass threshold of $0.7 \times 10^{14}\, h_{70}^{-1}\, M_\odot$ and $1.3 \times 10^{14}\, h_{70}^{-1}\, M_\odot$ (Tinker et al. 2008).

as we then fall below the required number of spectra for a good fit to the red-sequence model (see Appendix B of RM1). Nevertheless, the z_λ statistics of the validation catalog are equivalent to those of the full fiducial run.[60]

4.2. *Density of Clusters*

In Figure 6, we show the comoving density of redMaPPer clusters for DR8 (red) and SVA1 (blue). Densities are computed using our fiducial cosmology for clusters with $\lambda/S > 20$ by summing individual cluster $P(z)$ functions. The widths of the lines are smoothed over a redshift range $\delta z = 0.02$ and assume Poisson errors (which are consistent with jackknife errors). The black dashed line shows the predicted abundance for halos with $M_{500c} > 1 \times 10^{14}\, h_{70}^{-1}\, M_\odot$, with the dash–dotted lines showing the same with mass thresholds of $0.7 \times 10^{14}\, h_{70}^{-1}\, M_\odot$ and $1.3 \times 10^{14}\, h_{70}^{-1}\, M_\odot$ (Tinker et al. 2008).

We note that the redMaPPer cluster is volume limited only out to $z \leqslant 0.33$. Above this redshift, the cluster density as a function of redshift reflects two competing trends: an increasing Eddington (1913) bias in the estimated cluster richness, which tends to increase the cluster density as a function of richness, and an increasing detection threshold due to the shallow survey depth of the SDSS. For $z \approx 0.4$, the number of galaxies lost due to the shallow survey depth is relatively small, and Eddington bias dominates, leading to an apparent increase in the cluster density. As one moves toward even higher redshifts, the increasing detection threshold quickly dominates and the density of clusters falls as an increasing function of redshift.

The SVA1 density is roughly consistent with DR8 at low redshift, although the volume probed is much smaller; the peak at $z \sim 0.6$ is caused by the same Eddington bias effects as in DR8 at lower redshift. The number density slowly declines

[60] Though the z_λ statistics are the same, the richness estimations are not as stable, and thus our primary catalog utilizes all of the spectra for training.

with redshift in SVA1, which is consistent with a constant mass threshold at fixed richness. However, we caution that the possibility of a varying mass threshold (due to the build-up of the red sequence, for example) as well as Eddington bias and projection effects must be taken into account to compute a proper cluster abundance function $n(z, M)$ for cosmological studies.

5. EFFECTS OF STAR/GALAXY SEPARATION AND MASKING IN SVA1

As discussed in Section 2.1, the fiducial SVA1 redMaPPer footprint was based on the area used for the `ngmix` galaxy shape catalog, in order to utilize the improved morphological star/galaxy separation in this region. In addition, we removed 4% of the area with a relatively large concentration of centroid shifts between bandpasses in individual objects. However, these two choices come with some trade-offs. While the improvement in star/galaxy separation is clearly necessary in the selection of redMaGiC red galaxies (see Appendix A of RM15), it significantly reduced the footprint of the SVA1 redMaPPer catalog. This is especially detrimental for the purposes of comparing the redMaPPer catalog against external X-ray cluster catalogs (see Section 6.2). Similarly, while the bad region mask is clearly beneficial for shape measurements, it creates a footprint with many holes, which negatively impacts cluster centering. In this section, we investigate the impact of these choices on the richness and redshift recovery of redMaPPer clusters. We also describe an expanded redMaPPer catalog with a larger footprint that can be used for multi-wavelength cross-correlation measurements, increasing the number of clusters available in Section 6.2 by ∼50%.

5.1. Star/Galaxy Separation

The initial star/galaxy classifier in SVA1 data is the `modest` classifier based on the `SExtractor SPREAD_MODEL` quantity (Chang et al. 2015a; Jarvis et al. 2015, Section 2.2) which compares the fit of a point-spread function (PSF) model to that of a PSF convolved with a small circular exponential model for morphological classification. While the `modest` classifier works reasonably well at bright magnitudes, at $z \sim 0.7$ the stellar locus (in the DES optical bands *griz*) comes close to the galaxy red sequence. For accurate selection of individual red galaxies as in the redMaGiC catalog, this required our improved star/galaxy classification based on `ngmix` (Rozo et al. 2015c), which reduced stellar contamination from $\gtrsim$15% at $z \sim 0.7$ to less than 5%.

In order to estimate the impact of star/galaxy separation, we have rerun the redMaPPer cluster finder on a slightly expanded footprint using the `modest` star/galaxy classifier, while leaving everything else (including the red-sequence calibration) the same. We then match clusters from this catalog to our fiducial catalog. The first thing we find is that a small number of clusters (∼1.4%) are now badly miscentered on bright, red, misclassified stars (as determined from our improved star/galaxy separation from `ngmix`). We also note that the global background is slightly increased at high redshift, thus slightly depressing the richness estimates. The richness bias is ∼3% at $z = 0.8$, with the bias decreasing linearly with redshift such that the cluster richnesses at $z = 0.2$ are unbiased. We calibrate this bias with a simple linear model, and correct for it in our final expanded catalog. The associated systematic uncertainty in richness due to the inefficient star/galaxy separation is ∼2%, which is smaller than the statistical uncertainty on λ. Thus, aside from mild miscentering problems, redMaPPer richness estimates are quite insensitive to stellar contamination in the galaxy catalog, as expected.

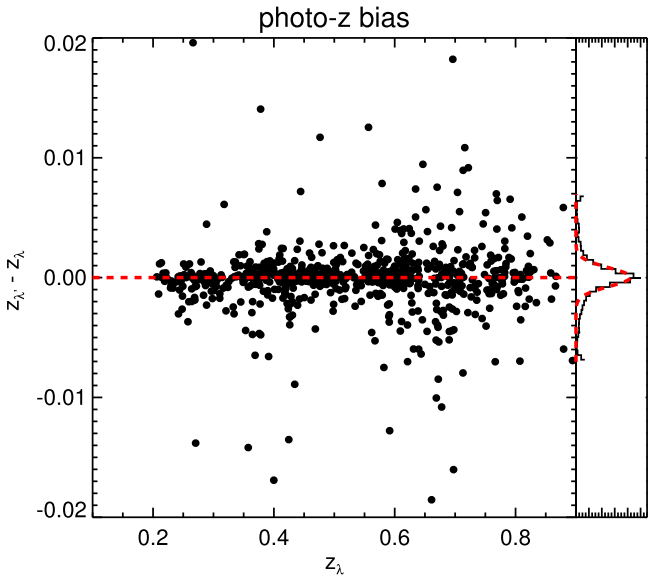

Figure 7. Plot of $\Delta z_\lambda = z_{\lambda'} - z_\lambda$ for the expanded ($z_{\lambda'}$) and fiducial (z_λ) catalogs. The cluster redshifts are very consistent, with few outliers at $\Delta z_\lambda > 0.01$, which is already $<1\sigma$ on the redshift error. The red dashed curve in the right panel is a Gaussian fit to the Δz_λ histogram, with mean 5×10^{-5} and rms 7×10^{-4}.

5.2. Masking

In addition to the overall geometric mask, our fiducial footprint includes masking for bright ($J < 13$) 2MASS stars and 4% of the area with a larger-than-typical concentration of object centroid shifts. However, we have found that several good cluster centers are masked in these regions, causing significant offsets from the X-ray and SZ centers (e.g., Section 2.3 of S15).

In order to estimate the impact of masking (in addition to star/galaxy separation), we have rerun redMaPPer on the expanded footprint using the `modest` classifier (as above) and including galaxies that had been rejected by both the 2MASS mask and the "4%" mask. We then match clusters from this expanded catalog to the fiducial catalog. Aside from those clusters which are now badly miscentered due to stellar contamination, two SPT clusters (SPT-CLJ0417–4748 and SPT-CL0456–5116; see S15) are now properly centered, as the central galaxies are no longer masked.

Figure 7 shows the comparison in cluster redshift z_λ between the expanded ($z_{\lambda'}$) and fiducial (z_λ) catalogs. The cluster redshifts are very consistent, with a few outliers at $\Delta z_\lambda > 0.01$. The red curve in the right panel shows a Gaussian fit to the Δz_λ histogram, with mean 5×10^{-5} and rms 7×10^{-4}. Thus, the worse star/galaxy separation and less conservative mask have no significant impact on the cluster redshift estimation.

Figure 8 shows the richness bias as the ratio of λ' (expanded catalog) to λ (fiducial catalog) in the SPT-E region. All values of λ' have been corrected for the star/galaxy separation bias model in Section 5.1. Again, the richness estimates are consistent, with a Gaussian fit showing $\lambda'/\lambda = 0.99 \pm 0.04$. We note that this

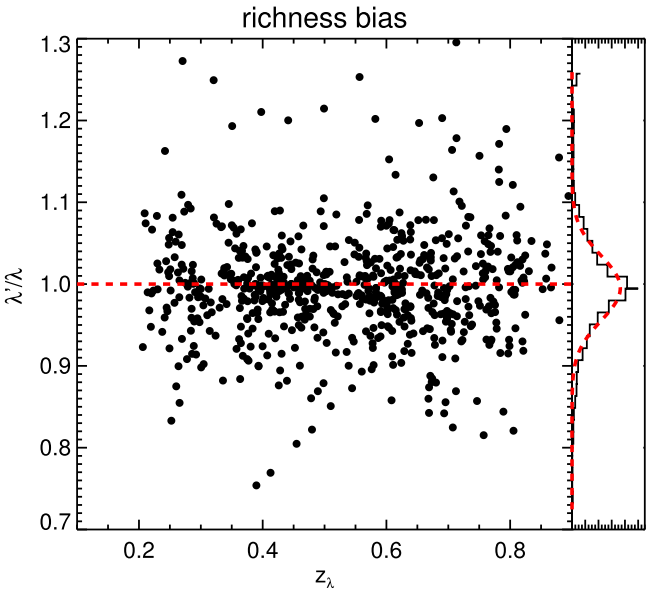

Figure 8. Plot of richness bias, λ'/λ, for the expanded (λ') and fiducial (λ) catalogs. All values of λ' have been corrected for the star/galaxy separation bias model in Section 5.1. The richness estimates are consistent, with a Gaussian fit (red dashed curve) showing $\lambda'/\lambda = 0.99 \pm 0.04$.

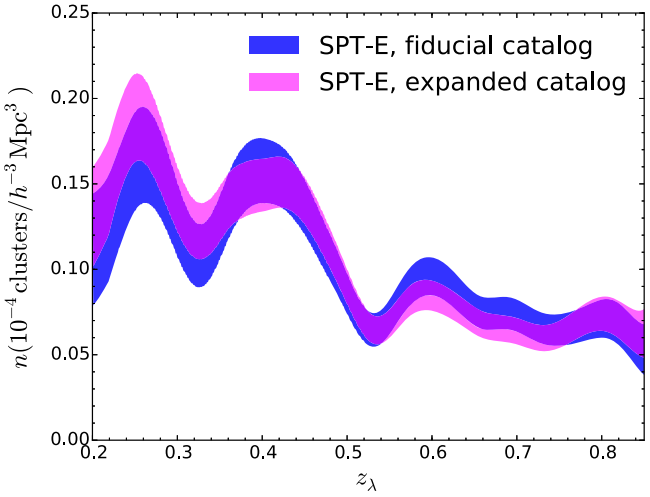

Figure 9. Number density of clusters for the expanded (magenta) and fiducial (blue) catalogs, limited to the SPT-E region. The number density is consistent within 1σ at all redshifts in spite of the changes in star/galaxy separation and masking.

~4% richness scatter is fully consistent with expectations based on the richness extrapolations in the fiducial catalog which made use of a more aggressive mask. However, we also find that for ~7% of clusters, λ'/λ differs from unity by more than 3σ. These apparent outliers are caused by clusters seen in projection. Changes in masking can change the way these projected clusters are deblended or merged by the redMaPPer algorithm, leading to these outliers. This result suggests a lower limit of ≈7% for the redMaPPer projection rate, and demonstrates the need for a full model of projection effects incorporated into a cluster abundance function.

In Figure 9, we show the comoving density of clusters in the SPT-E region for our fiducial (blue) and expanded (magenta) catalogs. The number densities are clearly consistent at all redshifts. Therefore, in future versions of redMaPPer on DES data, our fiducial runs will be performed with a less aggressive mask (with more area) as it has no impact on the richness estimation, yet it does improve cluster centering in a small number of cases. While improved star/galaxy separation is helpful for many purposes, it is heartening to know that our richness estimates are not strongly biased by a less-than-ideal separator. For this version of the catalog, however, we recommend that the fiducial catalog should be used for all purposes except where the greater area can be made use of in cross-checks with X-ray catalogs, as in Section 6.

6. THE CORRELATION OF REDMAPPER CLUSTER RICHNESS WITH X-RAY AND SZ GALAXY CLUSTER PROPERTIES

6.1. Correlation with the SPT SZ Cluster Catalog

A detailed comparison of the DES SVA1 redMaPPer and SPT SZ cluster catalogs has been published in S15. We briefly summarize their most important results. Using 129 deg^2 of overlapping data, they find 25 clusters between $0.1 < z < 0.8$, including 3 new clusters that did not have identified optical counterparts in Bleem et al. (2015). Every SZ cluster within the redMaPPer footprint and at $z < z_{\rm max}$ was detected in the redMaPPer catalog. Due to the high-mass threshold of the Bleem et al. (2015) sample, these are all high-mass and high-richness clusters, with a typical richness of $\lambda \sim 70$. Using the method of Bocquet et al. (2015), they implement a full likelihood formalism to constrain the λ–mass relation of SPT-selected clusters. By inverting the scaling relation from S15 using the methods of Evrard et al. (2014), they determine that the mass of a $\lambda \sim 20$ cluster is $M_{500c} \sim 10^{14}\, h_{70}^{-1}\, M_\odot$, which is consistent with the density of clusters from Section 4.2. In addition, they find a mass scatter at fixed richness, $\sigma_{\ln M|\lambda} = 0.18^{+0.08}_{-0.05}$, at a richness of $\lambda = 70$. Thus, they confirm that the redMaPPer richness λ is a low-scatter mass proxy for DES data across a much broader range in redshift than was probed in Rozo & Rykoff (2014). Furthermore, the parameters of the λ–mass relation are consistent with what was derived from SDSS DR8 data using a rough abundance matching argument (Rykoff et al. 2012), thus providing further confirmation of the fact that redMaPPer is probing a similar cluster population in SDSS and DES data.

In S15, they further constrain the optical-SZE positional offsets. The offset distribution is characterized by a two-component Gaussian model. The central component describes "well-centered" clusters where the optical and SZ positions are coincident (given the SZ positional uncertainty from the finite beam size of SPT). There is also a less populated tail of central galaxies with large offsets. For this work, we have modified the model such that the central Gaussian component is a one-dimensional rather than a two-dimensional Gaussian, as we have that found this produces superior χ^2 fits to the X-ray offsets in Section 6.2. The positional offsets, x, are now modeled as

$$p(x) = \frac{\rho_0}{\sigma_0\sqrt{2\pi}} e^{-\frac{x^2}{2\sigma_0^2}} + \frac{(1-\rho_0)x}{\sigma_1^2} e^{-\frac{x^2}{2\sigma_1^2}}, \quad (4)$$

where $x = r/R_\lambda$, ρ_0 is the fraction of the population with small offsets with variance σ_0^2, and the population with large offsets is characterized with variance σ_1^2. We have refit the offset model of SPT clusters from S15 r/R_λ rather than r/R_{500}, in addition to

using the redMaPPer positions from the expanded SVA1 catalog. This change allows us to better compare to the X-ray cluster samples described in Section 6.2. In all of the cases, we marginalize over the parameter σ_0 since it is not relevant to the overall fraction and distribution of incorrect central galaxies.

The optical-SZ positional offset distribution has a central component with $\rho_0 = 0.80^{+0.15}_{-0.37}$ and a large-offset population with $\sigma_1 = 0.27^{+0.21}_{-0.08} R_\lambda$. Given the matched clusters, the mean of the centering probability of the central galaxies of the clusters in the matched sample is $\langle P_{\rm cen} \rangle = 0.82$. This is consistent with the constraints from the optical-SZ matching, although the 21 clusters in the sample do not have a lot of constraining power.

6.2. Correlation with X-Ray Galaxy Clusters

In this section, we make use of the overlap of the redMaPPer SVA1 expanded catalog with X-ray observations from *Chandra* and *XMM* to measure the T_X–λ relation as well as to further constrain the centering properties of the catalog. More extensive comparisons to X-ray observations, including a full analysis of the redMaPPer DR8 catalog, will be presented in D. Hollowood et al. (2016, in preparation) and A. Bermeo-Hernandez et al. (2016, in preparation).

6.2.1. Chandra Analysis

The *Chandra* analysis was performed using a custom pipeline (see D. Hollowood et al. 2016, in preparation). A brief overview is given here. The pipeline is based on a series of CIAO (version 4.7; Fruscione et al. 2006) and HEASOFT (version 6.17) tools; all spectral fitting was performed using *XSPEC* (version 12.9.0, Arnaud 1996).

The *Chandra* pipeline was used to extract temperatures and luminosities from a list of clusters that were both in the redMaPPer catalog ($\lambda > 20$) and in at least one *Chandra* archival observation. The pipeline took a list of cluster positions, redshifts, and richnesses from the redMaPPer SVA1 expanded catalog, and queried the *Chandra* archive for observations of these positions using the *find_chandra_obsid* CIAO tool. The pipeline then downloaded each observation which contained a redMaPPer cluster, and re-reduced it using the *chandra_repro* CIAO tool.

Each observation was then cleaned using a standard X-ray analysis: the energy was cut to 0.3–7.9 keV, flares were removed using the *deflare* CIAO tool with the *lc_clean* algorithm, and point sources were removed using the *wavdetect* CIAO tool. A 500 kpc radius was then calculated around the redMaPPer center using the redMaPPer redshift z_λ and assuming a cosmology of $\Omega_m = 0.3$, $H_0 = 0.7$. This region was then iteratively recentered to the local X-ray centroid. At this point, the signal-to-noise ratio in this region was measured, and if it was less than 3.0, then analysis stopped. Otherwise, a spectrum was extracted from this region.

A temperature was then fit to this spectrum using a `WABS × MEKAL` model (Mewe et al. 1985), fixing the hydrogen column density to the Dickey & Lockman (1990) value from the *nH* HEASOFT tool, and the metal abundance to 0.3 times solar. An r_{2500} radius was derived from this temperature via the empirical relation found in Arnaud et al. (2005). The derived r_{2500} radius was then used to create an iteratively-centered r_{2500} region, which was then used to produce a new r_{2500} temperature and radius. The temperature and radii were then iterated until they converged within 1σ. Unabsorbed soft-band (0.5–2.0 keV) and bolometric (0.001–100 keV) luminosities were then calculated for the data.

In the redMaPPer expanded SVA1 sample, 61 clusters fell within a *Chandra* archival region, 38 of which had a sufficient signal to noise to be analyzed. Of these 38 clusters, 15 had sufficient statistics to fit an r_{2500} temperature. Finally, we reject one cluster from the comparison where the X-ray centroid is in a region of the redMaPPer footprint with $f_{\rm mask} > 0.2$. The cluster positions and temperatures used in this work are described in Table 3.

6.2.2. XCS Analysis

The *XMM-Newton* (*XMM*) analysis was performed using an adaption of the pipeline developed for the *XMM* Cluster Survey (XCS; Mehrtens et al. 2012). XCS uses all of the available data in the *XMM* public archive to search for galaxy clusters that were detected serendipitously in *XMM* images. X-ray sources are detected in *XMM* images using an algorithm based on wavelet transforms (see Lloyd-Davies et al. 2011, for details, LD11 hereafter). Sources are then compared to a model of the instrument PSF to determine if they are extended. Extended sources are flagged as cluster candidates because most extended X-ray sources are clusters (the remainder being low-redshift galaxies or supernova remnants).

We have matched all of the XCS cluster candidates within $1.5\,h^{-1}$ Mpc of a redMaPPer SVA1 cluster with $\lambda > 5$ (assuming the candidate lies at the redMaPPer determined redshift), although we note that all of the verified matches were within $0.4\,h^{-1}$ Mpc. We note that for this match, the default XCS-defined X-ray center was used (see LD11 for more information about XCS centroiding). If multiple matches are made, then only the closest match is retained. The initial matched sample contains 66 objects that passed XCS quality standards. An average X-ray temperature estimate for each cluster was then calculated for these objects using a method very similar to that described in LD11. The XCS T_X pipeline uses XSPEC (Arnaud 1996) to fit a `WABS × MEKAL` model (Mewe et al. 1985), fixing the hydrogen column density to the Dickey & Lockman (1990) value and the metal abundance to 0.3 times the solar value. For the study presented herein, differences compared to the LD11 version of the pipeline include the use of updated *XMM* calibration and XSPEC (12.8.1 g) versions, and the extraction of T_X values within r_{2500} regions. We compute r_{2500} using the same method as in Section 6.2.1. Of the 66 matches between XCS cluster candidates and redMaPPer SVA1, we obtain $T_{X,2500}$ values for 31, with the remainding clusters detected with insufficient signal to noise. We have checked the SVA1 images of each of these 31, with and without *XMM* flux contours overlaid. After doing so, we discarded 6 objects because the XCS to redMaPPer match was clearly serendipitous. Finally, we select only those clusters with $\lambda > 20$, and we reject four clusters from the comparison where the X-ray centroid is in a region of the redMaPPer footprint with $f_{\rm mask} > 0.2$. Our final sample of XCS clusters with positions (29) and the subset with T_X estimates (14) used in this work are described in Table 4.

6.2.3. The T_X–λ Relation

For this study, we wished to determine the redMaPPer $T_{X,2500}$–λ relation using clusters with either *XMM* or *Chandra* observations. However, it is well known that X-ray cluster

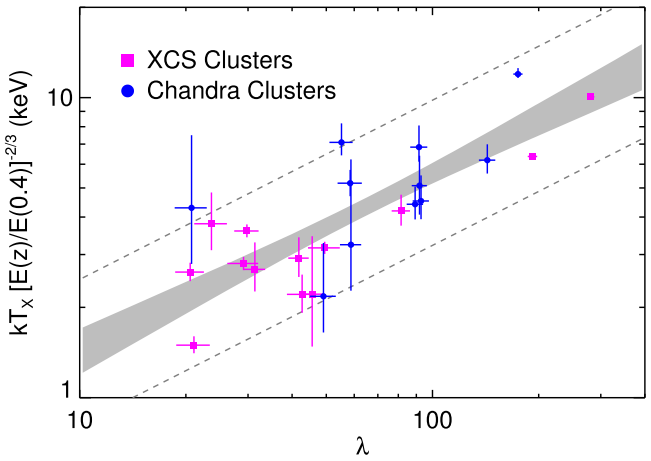

Figure 10. T_X–λ scaling relation derived from XCS (magneta squares) and *Chandra* (blue circles) clusters. All *Chandra* temperatures have been corrected according to Equation (5). The gray band shows the best-fit ($\pm 1\sigma$) scaling relation, and the dashed gray lines show $2\sigma_{\rm int}$ intrinsic scatter constraints.

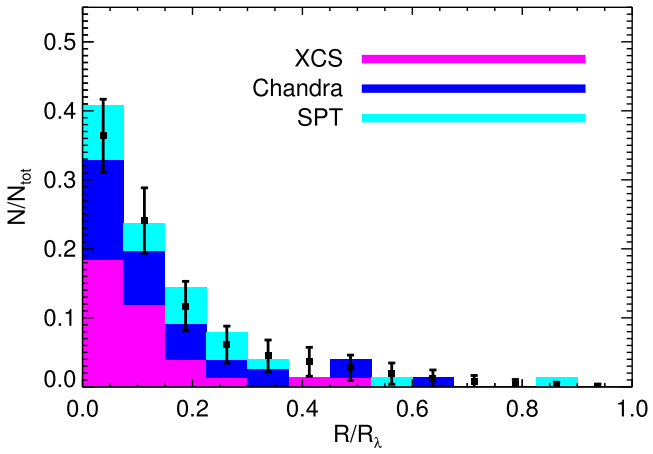

Figure 11. Histogram of positional offsets for the combined cluster sample as a function of R/R_λ. XCS clusters are shown in magenta, *Chandra* clusters in blue, and SPT clusters in cyan. The best-fit offset model, binned according to the data, is shown with black points. For reference, the average value of $\langle R_\lambda \rangle = 0.85\ h^{-1}$ Mpc, and the largest cluster offset is $0.75\ h^{-1}$ Mpc.

Table 2
redMaPPerCentral Offset Fits

Sample	No.	$\langle P_{\rm cen} \rangle$	ρ_0	$\sigma_1(R/R_\lambda)$	χ^2/dof
SPT	21	0.83	$0.80^{+0.15}_{-0.37}$	$0.27^{+0.21}_{-0.08}$	6.0/10
Chandra	35	0.80	$0.68^{+0.22}_{-0.18}$	$0.27^{+0.12}_{-0.05}$	4.7/10
XCS	29	0.82	$0.85^{+0.07}_{-.11}$	$0.22^{+0.08}_{-0.04}$	9.1/10
Combined	74	0.81	$0.78^{+0.11}_{-0.11}$	$0.31^{+0.09}_{-0.05}$	9.9/10

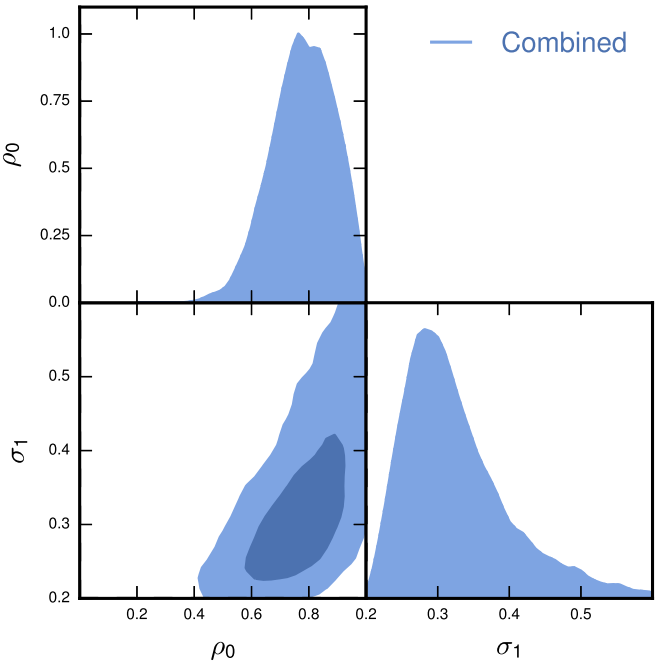

Figure 12. Posterior distribution for the 1σ and 2σ levels of two of the parameters ($\rho 0$, σ_1) from the positional offset model in Equation (4), for the combined XCS, *Chandra*, and SPT data. Best-fit parameters are shown in Table 2. The predicted well-centered fraction determined from redMaPPer centering probabilities is $\langle P_{\rm cen} \rangle = 0.82$, which is consistent with the best-fit value.

temperatures derived from *XMM* are systematically offset from *Chandra* observations (e.g., Schellenberger et al. 2015). Therefore, we have determined a correction factor to make the *Chandra* and *XMM* temperatures consistent. For this, we required access to more redMaPPer clusters with X-ray observations than are available in DES SVA1. We rely on recent compilations of T_X measurements of SDSS redMaPPer clusters using *Chandra* (D. Hollowood et al. 2016, in preparation) and *XMM* (A. Bermeo-Hernandez et al. 2016, in preparation). There are 41 DR8 redMaPPer clusters in common between these samples, allowing us to fit a correction factor of the form

$$\log_{10}\left(\frac{T_X^{Chandra}}{1\ \rm keV}\right) = 1.0133 \log_{10}\left(\frac{T_X^{XMM}}{1\ \rm keV}\right) + 0.1008 \qquad (5)$$

using BCES orthogonal fitting (Akritas & Bershady 1996). We note that this relation is consistent with that found by Schellenberger et al. (2015). Of the 14 redMaPPer SVA1 clusters with $T^{\rm XMM}_{X,2500}$ values, 4 are in common with the *Chandra* sample. From these 4, we have used the $T_{X,2500}$ value with the lowest uncertainty (3 from *XMM* and 1 from *Chandra*).

Figure 10 shows the T_X–λ scaling relation derived from XCS and *Chandra* clusters. All *Chandra* temperatures have been corrected according to Equation (5). We use an MCMC to fit the full cluster sample to a power-law model:

$$\ln(T_X) = \alpha + \beta \ln(\lambda/50) + \gamma \ln[E(z)/E(0.4)], \qquad (6)$$

with intrinsic scatter $\sigma_{\ln T|\lambda}$. Given the limited number of clusters in our sample, we fix the redshift evolution parameter $\gamma = -2/3$, assuming self-similar evolution. We find that $\alpha = 1.31 \pm .07$, $\beta = 0.60 \pm 0.09$, and $\sigma = 0.28^{+0.07}_{-0.05}$. The best-fit scaling relation (including 1σ error) is shown with the gray bar in Figure 10, and the dashed lines show the $\pm 2\sigma_{\ln T|\lambda}$ constraints. We note that the slope is consistent with $\beta = 2/3$, which is what we expect if clusters are self-similar and $\lambda \propto M$, as in S15.

S15 used SZ-selected clusters to place a constraint on the scatter in mass at fixed richness $\sigma_{\ln M|\lambda} = 0.18^{+0.08}_{-0.05}$. To compare against S15, we transform our constraints on the scatter in T_X at fixed mass to constraints on scatter in mass at

Table 3
Chandra Clusters

Name	ID[a]	λ	z_λ	α_{CG}	δ_{CG}	α_X	δ_X	T_X	Notes
CXOU J224845.1-443144	2	174.7 ± 5.2	0.372 ± 0.009	342.237888	−44.502977	342.187790	−44.528860	$15.35^{+0.73}_{-0.45}$	⋯
CXOU J051635.7-543042	4	192.1 ± 5.9	0.325 ± 0.016	79.154972	−54.516379	79.148935	−54.511790	$11.24^{+0.83}_{-0.84}$	1, 2
CXOU J004050.0-440757	8	143.0 ± 7.7	0.366 ± 0.009	10.208206	−44.130624	10.208210	−44.132540	$7.83^{+1.03}_{-0.77}$	1
CXOU J042605.0-545505	20	91.9 ± 4.5	0.642 ± 0.011	66.517163	−54.925298	66.520710	−54.918000	$7.57^{+1.98}_{-1.53}$	⋯
CXOU J045628.4-511640	38	91.6 ± 5.1	0.569 ± 0.007	74.117138	−51.276405	74.118490	−51.277660	$9.80^{+1.80}_{-1.05}$	⋯
CXOU J044148.1-485521	45	89.3 ± 4.8	0.812 ± 0.012	70.449577	−48.923361	70.450580	−48.922623	$7.19^{+1.06}_{-0.80}$	1
CXOU J044905.8-490131	54	92.8 ± 4.9	0.800 ± 0.012	72.266860	−49.027566	72.274050	−49.025320	$7.33^{+1.61}_{-0.97}$	1
CXOU J041804.1-475001	143	52.6 ± 3.4	0.584 ± 0.007	64.523720	−47.827636	64.516980	−47.833660	⋯	⋯
CXOU J095736.6+023427	183	58.4 ± 4.6	0.381 ± 0.009	149.404209	2.573747	149.402610	2.574050	$6.61^{+0.72}_{-0.64}$	2
CXOU J045314.4-594426	211	46.8 ± 4.4	0.315 ± 0.018	73.336516	−59.723625	73.310150	−59.740450	⋯	⋯
CXOU J043939.5-542420	260	58.7 ± 4.1	0.682 ± 0.015	69.916567	−54.403846	69.914690	−54.405470	$4.89^{+4.61}_{-1.47}$	⋯
CXOU J050921.2-534211	269	55.2 ± 4.2	0.461 ± 0.009	77.371828	−53.707888	77.338340	−53.703120	$9.54^{+1.52}_{-0.92}$	⋯
CXOU J044646.2-483336	353	48.5 ± 3.9	0.773 ± 0.014	71.693121	−48.558086	71.692480	−48.560120	⋯	⋯
CXOU J095902.5+025534	380	42.7 ± 4.0	0.366 ± 0.011	149.761335	2.929103	149.760330	2.926170	$4.03^{+0.65}_{-0.59}$	2
CXOU J100047.6+013940	388	29.8 ± 2.4	0.209 ± 0.005	150.189817	1.657398	150.198335	1.661128	$3.49^{+0.17}_{-0.16}$	2
CXOU J042741.7-544559	516	49.1 ± 4.1	0.435 ± 0.010	66.900538	−54.768035	66.923670	−54.766510	$2.84^{+1.46}_{-0.70}$	⋯
CXOU J045232.9-594528	578	28.1 ± 2.8	0.266 ± 0.015	73.072468	−59.741317	73.137020	−59.757810	⋯	⋯
CXOU J065638.9-555819	767	28.9 ± 3.0	0.269 ± 0.015	104.145859	−55.977785	104.161980	−55.972045	⋯	⋯
CXOU J034031.0-284834	1054	23.2 ± 2.6	0.475 ± 0.011	55.129143	−28.817229	55.129200	−28.809310	⋯	⋯
CXOU J010258.1-493019	1156	26.4 ± 2.5	0.711 ± 0.022	15.701349	−49.511298	15.741875	−49.505220	⋯	⋯
CXOU J004137.9-440225	1227	26.7 ± 2.9	0.459 ± 0.011	10.403128	−44.040263	10.407830	−44.040270	⋯	⋯
CXOU J003309.7-434745	1245	22.6 ± 2.5	0.407 ± 0.010	8.282083	−43.799248	8.290260	−43.795940	⋯	2
CXOU J045628.1-454024	1371	20.3 ± 2.1	0.578 ± 0.009	74.110967	−45.672684	74.117070	−45.673420	⋯	⋯
CXOU J022428.2-041529	1474	21.1 ± 2.3	0.254 ± 0.013	36.138450	−4.238674	36.117590	−4.258110	⋯	2
CXOU J034107.3-284559	1527	21.4 ± 2.1	0.589 ± 0.011	55.286213	−28.774285	55.280510	−28.766290	⋯	⋯
CXOU J100107.1+013408	1635	29.0 ± 3.4	0.381 ± 0.013	150.298618	1.554297	150.279780	1.569010	⋯	2
CXOU J022018.9-055647	1775	26.7 ± 3.1	0.660 ± 0.018	35.085095	−5.950116	35.078740	−5.946320	⋯	⋯
CXOU J044245.8-485443	1919	24.4 ± 2.8	0.820 ± 0.015	70.692931	−48.912217	70.690843	−48.911910	⋯	⋯
CXOU J044833.6-485007	1976	20.8 ± 2.2	0.421 ± 0.021	72.138634	−48.836412	72.140030	−48.835250	$5.59^{+4.24}_{-1.98}$	⋯
CXOU J044736.8-584530	2114	24.0 ± 2.6	0.681 ± 0.020	71.878993	−58.756044	71.903350	−58.758450	⋯	⋯
CXOU J095835.9+021235	2312	25.3 ± 3.5	0.944 ± 0.017	149.649663	2.209287	149.649662	2.209640	⋯	⋯
CXOU J045240.1-531552	2387	23.1 ± 2.8	0.687 ± 0.024	73.169362	−53.263914	73.167080	−53.264510	⋯	⋯
CXOU J095957.5+021825	2453	23.5 ± 2.9	0.923 ± 0.016	149.987795	2.315731	149.989540	2.306938	⋯	⋯
CXOU J100158.5+020352	2883	23.5 ± 3.4	0.441 ± 0.012	150.490085	2.069402	150.493733	2.064392	⋯	⋯
CXOU J045553.2-510748	3145	24.5 ± 3.0	0.756 ± 0.024	73.971873	−51.129557	73.971810	−51.130120	⋯	⋯

Notes. (1) Also in SPT catalog (S15). (2) Also in XCS catalog (see Table 4).
[a] ID in expanded SVA1 catalog.

fixed richness by assuming a self-similar slope $T_X \propto M^{2/3}$. We also require an estimate for the scatter in mass at fixed X-ray temperature when T_X is not core-excised. We rely on the results by Lieu et al. (2015), who find an intrinsic scatter in weak-lensing mass at a fixed temperature of $\sigma_{\ln M_{WL}|T} = 0.41$. Our choice is motivated by the fact this study, like ours, measures cluster temperatures with no core-excision. Adopting a 25% intrinsic scatter in weak-lensing mass at fixed mass, we arrive at an intrinsic scatter in mass at fixed temperature $\sigma_{\ln M|T} = 0.32$. Finally, given that the X-ray cluster sample extends to low-richness systems, which are expected to have a larger scatter, we adopt a richness-dependent scatter as a function of mass:

$$\mathrm{Var}(\ln\lambda|M) = \langle\lambda|M\rangle^{-1} + \sigma^2_{\ln\lambda|M}. \quad (7)$$

Following Evrard et al. (2014), we arrive at $\sigma_{\ln M|\lambda} = 0.3 \pm 0.15$. This result is higher than but consistent with that of S15. The large error bars reflect in part the large intrinsic scatter in the mass–T_X relation for non-core-excised temperatures.

6.2.4. Positional Offset Distribution

Using each of the SPT, *Chandra*, and XCS redMaPPer-matched samples, we have fit the positional offset model of Equation (4). For the SZ sample, the error on the position was given by Equation (11) from S15; for the X-ray samples, we used a fixed error of 10″. However, we note that this does not fully account for systematic errors in X-ray centroids, especially for clusters with complex morphologies. For the X-ray samples, we do not require the cluster to be bright enough to obtain a temperature constraint in order for it to have a well-detected center.

The offset model results are summarized in Table 2 with errors quoted as 68% confidence intervals as derived from an Markov Chain Monte Carlo fit to the data, similar to Section 4.3 of S15. The constraints on ρ_0 and σ_1 (the large-offset "miscentered" component) are all consistent within errors for all three samples.

To better constrain the overall centering of the redMaPPer SVA1 expanded cluster sample, we have also performed a joint likelihood fit to all three cluster samples. In the cases where we

Table 4
XCS Clusters

Name	ID[a]	λ	z_λ	α_{CG}	δ_{CG}	α_X	δ_X	T_X	Notes
XMMXCS J065828.8-555640.8	1	281.2 ± 6.5	0.298 ± 0.017	104.646822	−55.949043	104.620400	−55.944680	$9.44^{+0.14}_{-0.14}$	⋯
XMMXCS J051636.6-543120.8	4	192.1 ± 5.9	0.325 ± 0.016	79.154972	−54.516379	79.152740	−54.522467	$6.08^{+0.10}_{-0.10}$	1, 2
XMMXCS J021441.2-043313.8	29	56.3 ± 3.6	0.139 ± 0.004	33.671242	−4.567278	33.671952	−4.553851	⋯	⋯
XMMXCS J044956.6-444017.3	32	55.4 ± 2.6	0.144 ± 0.003	72.485352	−44.673356	72.486117	−44.671479	⋯	1
XMMXCS J233227.2-535828.2	33	82.8 ± 4.1	0.424 ± 0.007	353.114476	−53.974433	353.113450	−53.974510	⋯	⋯
XMMXCS J095940.7+023110.8	74	81.5 ± 4.9	0.707 ± 0.015	149.923436	2.525051	149.919750	2.519675	$5.01^{+0.66}_{-0.54}$	⋯
XMMXCS J034005.2-285024.4	99	69.6 ± 4.8	0.344 ± 0.014	55.029953	−28.844377	55.021691	−28.840115	⋯	⋯
XMMXCS J224824.7-444225.3	136	63.0 ± 4.3	0.476 ± 0.010	342.098778	−44.708732	342.103250	−44.707049	⋯	⋯
XMMXCS J232956.5-560802.7	164	50.1 ± 3.1	0.418 ± 0.010	352.472225	−56.136006	352.485700	−56.134094	⋯	⋯
XMMXCS J095737.1+023428.9	183	58.4 ± 4.6	0.381 ± 0.009	149.404209	2.573747	149.404960	2.574713	$4.61^{0.59}_{-0.48}$	2
XMMXCS J003428.0-431854.2	274	49.5 ± 5.1	0.393 ± 0.010	8.614189	−43.316563	8.617005	−43.315066	$3.14^{+0.15}_{-0.14}$	⋯
XMMXCS J021734.7-051327.6	277	46.3 ± 3.3	0.658 ± 0.014	34.394127	−5.220327	34.394879	−5.224348	⋯	⋯
XMMXCS J045506.0-532342.4	299	41.8 ± 2.8	0.418 ± 0.010	73.773464	−53.396441	73.775354	−53.395126	$2.95^{+0.51}_{-0.40}$	⋯
XMMXCS J022511.8-062300.7	306	31.4 ± 2.2	0.215 ± 0.005	36.301178	−6.383116	36.299332	−6.383549	$2.38^{+0.55}_{-0.37}$	⋯
XMMXCS J095902.7+025544.9	380	42.7 ± 4.0	0.366 ± 0.011	149.761335	2.929103	149.761390	2.929155	$2.16^{+0.35}_{-0.29}$	2
XMMXCS J100047.3+013927.8	388	29.8 ± 2.4	0.209 ± 0.005	150.189817	1.657398	150.197330	1.657734	$3.18^{+0.16}_{-0.15}$	2
XMMXCS J233345.8-553826.9	451	45.6 ± 3.6	0.746 ± 0.019	353.441511	−55.637993	353.441180	−55.640811	$2.70^{+1.51}_{-0.89}$	⋯
XMMXCS J003346.3-431729.7	489	29.1 ± 2.9	0.214 ± 0.005	8.443268	−43.291959	8.442920	−43.291608	$2.49^{+0.13}_{-0.12}$	⋯
XMMXCS J232810.2-555015.8	889	40.1 ± 3.6	0.813 ± 0.014	352.031286	−55.839880	352.042820	−55.837728	⋯	⋯
XMMXCS J095901.2+024740.4	1193	20.4 ± 2.4	0.504 ± 0.012	149.756320	2.794723	149.755310	2.794571	⋯	⋯
XMMXCS J233000.5-543706.3	1198	20.6 ± 1.9	0.176 ± 0.004	352.501689	−54.618800	352.502360	−54.618431	$2.27^{+0.17}_{-0.15}$	⋯
XMMXCS J003309.8-434758.3	1245	22.6 ± 2.5	0.407 ± 0.010	8.282083	−43.799248	8.290958	−43.799532	⋯	2
XMMXCS J022827.3-042538.7	1434	23.6 ± 2.5	0.434 ± 0.014	37.115911	−4.435404	37.114008	−4.427436	$3.88^{+1.05}_{-0.71}$	⋯
XMMXCS J022433.9-041432.7	1474	21.1 ± 2.3	0.254 ± 0.013	36.138450	−4.238674	36.141298	−4.242430	$1.36^{+0.10}_{-0.08}$	2
XMMXCS J100109.1+013336.8	1635	29.0 ± 3.4	0.381 ± 0.013	150.298618	1.554297	150.288320	1.560238	⋯	2
XMMXCS J022307.9-041257.2	1707	20.0 ± 2.0	0.618 ± 0.013	35.794975	−4.214364	35.782951	−4.215907	⋯	⋯
XMMXCS J003627.6-432830.3	1868	23.5 ± 2.7	0.397 ± 0.015	9.109958	−43.453131	9.115160	−43.475104	⋯	⋯
XMMXCS J021755.3-052708.0	2833	21.8 ± 2.7	0.667 ± 0.021	34.475702	−5.451563	34.480539	−5.452240	⋯	⋯
XMMXCS J033931.8-283444.7	5590	21.1 ± 3.1	0.824 ± 0.015	54.901800	−28.575329	54.882578	−28.579090	⋯	⋯

Notes. (1) Also in SPT catalog. (2) Also in *Chandra* catalog.
[a] ID in expanded SVA1 catalog.

Table 5
redMaPPer Catalogs and Associated Products

Filename	Description	Table Reference
`redmapper_dr8_public_v6.3_catalog.fits`	SDSS DR8 catalog	Table 6
`redmapper_dr8_public_v6.3_members.fits`	SDSS DR8 members	Table 7
`redmapper_dr8_public_v6.3_zmask.fits`	SDSS DR8 z_{max} map	Table 10
`redmapper_dr8_public_v6.3_randoms.fits`	SDSS DR8 random points	Table 11
`redmapper_dr8_public_v6.3_area.fits`	SDSS DR8 effective area	Table 12
`redmapper_sva1_public_v6.3_catalog.fits`	DES SVA1 catalog	Table 8
`redmapper_sva1_public_v6.3_members.fits`	DES SVA1 members	Table 9
`redmapper_sva1-expanded_public_v6.3_catalog.fits`	DES SVA1 expanded catalog[a]	Table 8
`redmapper_sva1-expanded_public_v6.3_members.fits`	DES SVA1 expanded members[a]	Table 9
`redmapper_sva1_public_v6.3_zmask.fits`	DES SVA1 z_{max} map	Table 10
`redmapper_sva1_public_v6.3_randoms.fits`	DES SVA1 random points	Table 11
`redmapper_sva1_public_v6.3_area.fits`	DES SVA1 effective area	Table 12

Note.
[a] See Section 5.2.
(This table is available in its entirety in FITS format.)

have multiple observations of the same cluster, we first take the XCS position, followed by the *Chandra* position, followed by the SPT position. As our goal is to better constrain the well-centered fraction ρ_0 as well as the miscentering kernel σ_1, our joint likelihood constrains these two parameters for the full sample. However, to allow for differences in centering precision, we use a separate value of σ_0 for each individual sample. In all, we have five parameters, but we treat the set of $\{\sigma_0\}$ as nuisance parameters in our figures below.

The histogram of offsets for the combined sample is shown in Figure 11. The results of our joint fit are shown in Figure 12 and described in Table 2. The best-fit model has been binned to

Table 6
redMaPPer DR8 Cluster Catalog Format

Name	Data Type	Description
ID	INT(4)	redMaPPer Cluster Identification Number
NAME	CHAR(20)	redMaPPer Cluster Name
R.A.	FLOAT(8)	R.A. in decimal degrees (J2000)
decl.	FLOAT(8)	decl. in decimal degrees (J2000)
Z_LAMBDA	FLOAT(4)	Cluster photo-z z_λ
Z_LAMBDA_ERR	FLOAT(4)	Gaussian error estimate for z_λ
LAMBDA	FLOAT(4)	Richness estimate λ
LAMBDA_ERR	FLOAT(4)	Gaussian error estimate for λ
S	FLOAT(4)	Richness scale factor (see Equation (2))
Z_SPEC	FLOAT(4)	SDSS spectroscopic redshift for most likely center (-1.0 if not available)
OBJID	INT(8)	SDSS DR8 CAS object identifier
IMAG	FLOAT(4)	i-band cmodel magnitude for most likely central galaxy (dereddened)
IMAG_ERR	FLOAT(4)	error on i-band cmodel magnitude
MODEL_MAG_U	FLOAT(4)	u model magnitude for most likely central galaxy (dereddened)
MODEL_MAGERR_U	FLOAT(4)	error on u model magnitude
MODEL_MAG_G	FLOAT(4)	g model magnitude for most likely central galaxy (dereddened)
MODEL_MAGERR_G	FLOAT(4)	error on g model magnitude
MODEL_MAG_R	FLOAT(4)	r model magnitude for most likely central galaxy (dereddened)
MODEL_MAGERR_R	FLOAT(4)	error on r model magnitude
MODEL_MAG_I	FLOAT(4)	i model magnitude for most likely central galaxy (dereddened)
MODEL_MAGERR_I	FLOAT(4)	error on i model magnitude
MODEL_MAG_Z	FLOAT(4)	z model magnitude for most likely central galaxy (dereddened)
MODEL_MAGERR_Z	FLOAT(4)	error on z model magnitude
ILUM	FLOAT(4)	Total membership-weighted i-band luminosity (units of L_*)
P_CEN[5]	5 × FLOAT(4)	Centering probability $P_{\rm cen}$ for 5 most likely centrals
RA_CEN[5]	5 × FLOAT(8)	R.A. for 5 most likely centrals
DEC_CEN[5]	5 × FLOAT(8)	decl. for 5 most likely centrals
ID_CEN[5]	5 × INT(8)	DR8 CAS object identifier for 5 most likely centrals
PZBINS[21]	21 × FLOAT(4)	Redshift points at which $P(z)$ is evaluated
PZ[21]	21 × FLOAT(4)	$P(z)$ evaluated at redshift points given by PZBINS

match the data and is overplotted with black points in Figure 11. Our final constraint on the fraction of clusters that are correctly centered is $\rho_0 = 0.78^{+0.11}_{-0.11}$, compared to the redMaPPer predicted fraction of 0.82, which is in very good agreement. By comparison, redMaPPer clusters in SDSS are correctly centered ≈86% of the time (see Rozo & Rykoff 2014).

7. SUMMARY

We present the DES SVA1 redMaPPer cluster catalog and an updated version of the SDSS redMaPPer cluster catalog. Relative to the last redMaPPer public release (v5.10, see RM4), this new version (v6.3) includes a variety of improvements, specifically noted below.

1. The algorithm now makes use of the depth maps generated as per Rykoff et al. (2015) to properly account for small-scale structure in the survey properties.
2. The synthetic curves for passive evolutions used by redMaPPer are now internally generated using the BC03 model.
3. The selection of initial candidate red galaxies has been improved, allowing redMaPPer to internally self calibrate with sparser spectroscopic data.
4. The catalog has a position-dependent redshift reach determined from the underlying survey inhomogeneity.
5. We have updated our generation of random points to properly account for the above changes, particularly the position-dependent redshift reach of the cluster catalog.

As with previous releases, the photometric redshift performance of the SDSS catalogs is superb, being nearly unbiased and with photometric redshift scatter $\sigma_z/(1+z) \leqslant 0.01$, except for the most distant clusters. Photometric redshift performance in DES SV is also excellent, with a scatter $\sigma_z/(1+z) \approx 0.01$, only now the redshift range of the cluster catalog extends to $z = 0.9$. The cluster richness has been shown to be tightly correlated with cluster mass (≈20% scatter) by S15. We have further validated this tight scatter using X-ray scaling relations. These analyses, as well as the comoving density of galaxy clusters in DES SVA1, suggest that the DES SVA1 detection threshold corresponds to a limiting mass $M_{500c} \approx 10^{-14}\, h^{-1}\, M_\odot$ for our high-quality $\lambda > 20$ cluster sample.

Finally, we have investigated the miscentering distribution of the DES SV clusters. The current data place only modest constraints on the miscentering distribution, and we find that the fraction of clusters that are correctly centered is ≈0.78 ± 0.11, which is fully consistent with our expectations from the redMaPPer centering probabilities, $P_{\rm cen}$.

Our results demonstrate that the DES imaging data is sufficiently robust and of sufficient quality to pursue photometric cluster finding up to redshift $z = 0.9$, with well controlled selection functions, richness measurements, and

Table 7

redMaPPer DR8 Member Catalog Format

Name	Format	Description
ID	INT(4)	redMaPPer Cluster Identification Number
R.A.	FLOAT(8)	R.A. in decimal degrees (J2000)
decl.	FLOAT(8)	decl. in decimal degrees (J2000)
R	FLOAT(4)	Distance from cluster center (h^{-1} Mpc)
P	FLOAT(4)	Membership probability
P_FREE	FLOAT(4)	Probability that member is not a member of a higher ranked cluster
THETA_L	FLOAT(4)	Luminosity (i-band) weight
THETA_R	FLOAT(4)	Radial weight
IMAG	FLOAT(4)	i-band cmodel magnitude (dereddened)
IMAG_ERR	FLOAT(4)	error on i-band cmodel magnitude
MODEL_MAG_U	FLOAT(4)	u model magnitude (dereddened)
MODEL_MAGERR_U	FLOAT(4)	error on u model magnitude
MODEL_MAG_G	FLOAT(4)	g model magnitude (dereddened)
MODEL_MAGERR_G	FLOAT(4)	error on g model magnitude
MODEL_MAG_R	FLOAT(4)	r model magnitude (dereddened)
MODEL_MAGERR_R	FLOAT(4)	error on r model magnitude
MODEL_MAG_I	FLOAT(4)	i model magnitude (dereddened)
MODEL_MAGERR_I	FLOAT(4)	error on i model magnitude
MODEL_MAG_Z	FLOAT(4)	z model magnitude (dereddened)
MODEL_MAGERR_Z	FLOAT(4)	error on z model magnitude
Z_SPEC	FLOAT(4)	SDSS spectroscopic redshift (-1.0 if not available)
OBJID	INT(8)	SDSS DR8 CAS object identifier

Note. The probability p is the raw membership probability, while the probability $p_{\rm free}$ is the probability that the galaxy does not belong to a previous cluster in the percolation. The total membership probability must be modified by the radial and luminosity weights, such that $p_{\rm mem} = p \times p_{\rm free} \times \theta_i \times \theta_r$.

excellent photometric redshift performance, setting the stage for upcoming analyses and cluster abundance constraints with the largest cluster samples available to date.

This paper has gone through internal review by the DES collaboration. We are grateful for the extraordinary contributions of our CTIO colleagues and the DECam Construction, Commissioning, and SV teams in achieving the excellent instrument and telescope conditions that have made this work possible. The success of this project also relies critically on the expertise and dedication of the DESDM group.

This work was supported in part by the U.S. Department of Energy contract to SLAC No. DE-AC02-76SF00515, as well as DOE grants DE-SC0007093 (DH) and DE-SC0013541 (DH and TJ).

Funding for the DES Projects has been provided by the U.S. Department of Energy, the U.S. National Science Foundation, the Ministry of Science and Education of Spain, the Science and Technology Facilities Council of the United Kingdom, the Higher Education Funding Council for England, the National Center for Supercomputing Applications at the University of Illinois at Urbana-Champaign, the Kavli Institute of Cosmological Physics at the University of Chicago, the Center for Cosmology and Astro-Particle Physics at the Ohio State University, the Mitchell Institute for Fundamental Physics and Astronomy at Texas A&M University, Financiadora de Estudos e Projetos, Fundação Carlos Chagas Filho de Amparo à Pesquisa do Estado do Rio de Janeiro, Conselho Nacional de Desenvolvimento Científico e Tecnológico and the Ministério da Ciência, Tecnologia e Inovação, the Deutsche Forschungsgemeinschaft, and the Collaborating Institutions in the Dark Energy Survey.

The Collaborating Institutions are Argonne National Laboratory, the University of California at Santa Cruz, the University of Cambridge, Centro de Investigaciones Energéticas, Medioambientales y Tecnológicas-Madrid, the University of Chicago, University College London, the DES-Brazil Consortium, the University of Edinburgh, the Eidgenössische Technische Hochschule (ETH) Zürich, Fermi National Accelerator Laboratory, the University of Illinois at Urbana-Champaign, the Institut de Ciències de l'Espai (IEEC/CSIC), the Institut de Física d'Altes Energies, Lawrence Berkeley National Laboratory, the Ludwig-Maximilians Universität München and the associated Excellence Cluster universe, the University of Michigan, the National Optical Astronomy Observatory, the University of Nottingham, The Ohio State University, the University of Pennsylvania, the University of Portsmouth, SLAC National Accelerator Laboratory, Stanford University, the University of Sussex, and Texas A&M University.

The DES data management system is supported by the National Science Foundation under grant No. AST-1138766. The DES participants from Spanish institutions are partially supported by MINECO under grants AYA2012-39559, ESP2013-48274, FPA2013-47986, and Centro de Excelencia Severo Ochoa SEV-2012-0234. Research leading to these results has received funding from the European Research Council under the European Unions Seventh Framework Programme (FP7/2007-2013) including ERC grant agreements 240672, 291329, and 306478.

Based in part on observations taken at the Australian Astronomical Observatory under program A/2013B/012.

Funding for SDSS-III has been provided by the Alfred P. Sloan Foundation, the Participating Institutions, the National Science Foundation, and the U.S. Department of Energy Office of Science. The SDSS-III web site is http://www.sdss3.org/.

SDSS-III is managed by the Astrophysical Research Consortium for the Participating Institutions of the SDSS-III Collaboration including the University of Arizona, the Brazilian Participation Group, Brookhaven National Laboratory, University of Cambridge, Carnegie Mellon University, University of Florida, the French Participation Group, the German Participation Group, Harvard University, the Instituto de Astrofisica de Canarias, the Michigan State/Notre Dame/JINA Participation Group, Johns Hopkins University, Lawrence Berkeley National Laboratory, Max Planck Institute for Astrophysics, Max Planck Institute for Extraterrestrial Physics, New Mexico State University, New York University, Ohio State University, Pennsylvania State University, University of Portsmouth, Princeton University, the Spanish Participation Group, University of Tokyo, University of Utah, Vanderbilt University, University of Virginia, University of Washington, and Yale University.

This publication makes use of data products from the Two Micron All Sky Survey, which is a joint project of the University of Massachusetts and the Infrared Processing and Analysis Center/California Institute of Technology, funded by the National Aeronautics and Space Administration and the National Science Foundation.

Table 8
redMaPPer SVA1 Cluster Catalog Format

Name	Format	Description
ID	INT(4)	redMaPPer Cluster Identification Number
NAME	CHAR(20)	redMaPPer Cluster Name
R.A.	FLOAT(8)	R.A. in decimal degrees (J2000)
decl.	FLOAT(8)	decl. in decimal degrees (J2000)
Z_LAMBDA	FLOAT(4)	Cluster photo-z z_λ
Z_LAMBDA_ERR	FLOAT(4)	Gaussian error estimate for z_λ
LAMBDA	FLOAT(4)	Richness estimate λ
LAMBDA_ERR	FLOAT(4)	Gaussian error estimate for λ
S	FLOAT(4)	Richness scale factor (see Equation (2))
Z_SPEC	FLOAT(4)	SDSS spectroscopic redshift for most likely center (-1.0 if not available)
COADD_OBJECTS_ID	INT(8)	DES `COADD_OBJECTS_ID` identification number
MAG_AUTO_G	FLOAT(4)	g MAG_AUTO magnitude for most likely central galaxy (SLR corrected)
MAGERR_AUTO_G	FLOAT(4)	error on g MAG_AUTO magnitude
MAG_AUTO_R	FLOAT(4)	r MAG_AUTO magnitude for most likely central galaxy (SLR corrected)
MAGERR_AUTO_R	FLOAT(4)	error on g MAG_AUTO magnitude
MAG_AUTO_I	FLOAT(4)	i MAG_AUTO magnitude for most likely central galaxy (SLR corrected)
MAGERR_AUTO_I	FLOAT(4)	error on g MAG_AUTO magnitude
MAG_AUTO_Z	FLOAT(4)	z MAG_AUTO magnitude for most likely central galaxy (SLR corrected)
MAGERR_AUTO_Z	FLOAT(4)	error on g MAG_AUTO magnitude
ZLUM	FLOAT(4)	Total membership-weighted z-band luminosity (units of L_*)
P_CEN[5]	5 × FLOAT(4)	Centering probability $P_{\rm cen}$ for 5 most likely centrals
RA_CEN[5]	5 × FLOAT(8)	R.A. for 5 most likely centrals
DEC_CEN[5]	5 × FLOAT(8)	decl. for 5 most likely centrals
ID_CEN[5]	5 × INT(8)	DES `COADD_OBJECTS_ID` identification number for 5 most likely centrals
PZBINS[21]	21 × FLOAT(4)	Redshift points at which $P(z)$ is evaluated
PZ[21]	21 × FLOAT(4)	$P(z)$ evaluated at redshift points given by PZBINS

Table 9
redMaPPer DES SVA1 Member Catalog Format

Name	Format	Description
ID	INT(4)	redMaPPer Cluster Identification Number
R.A.	FLOAT(8)	R.A. in decimal degrees (J2000)
decl.	FLOAT(8)	decl. in decimal degrees (J2000)
R	FLOAT(4)	Distance from cluster center (h^{-1} Mpc)
P	FLOAT(4)	Membership probability
P_FREE	FLOAT(4)	Probability that member is not a member of a higher ranked cluster
THETA_L	FLOAT(4)	Luminosity (z band) weight
THETA_R	FLOAT(4)	Radial weight
MAG_AUTO_G	FLOAT(4)	g MAG_AUTO magnitude (SLR corrected)
MAGERR_AUTO_G	FLOAT(4)	error on g MAG_AUTO magnitude
MAG_AUTO_R	FLOAT(4)	r MAG_AUTO magnitude (SLR corrected)
MAGERR_AUTO_R	FLOAT(4)	error on r MAG_AUTO magnitude
MAG_AUTO_I	FLOAT(4)	i MAG_AUTO magnitude (SLR corrected)
MAGERR_AUTO_I	FLOAT(4)	error on i MAG_AUTO magnitude
MAG_AUTO_Z	FLOAT(4)	z MAG_AUTO magnitude (SLR corrected)
MAGERR_AUTO_Z	FLOAT(4)	error on z MAG_AUTO magnitude
Z_SPEC	FLOAT(4)	Spectroscopic redshift (-1.0 if not available)
COADD_OBJECTS_ID	INT(8)	DES `COADD_OBJECTS_ID` identification number

Note. See Table 7 for information on how to compute $p_{\rm mem}$.

GAMA is a joint European-Australasian project based around a spectroscopic campaign using the Anglo-Australian Telescope. The GAMA input catalog is based on data taken from the Sloan Digital Sky Survey and the UKIRT Infrared Deep Sky Survey. Complementary imaging of the GAMA regions is being obtained by a number of independent survey programmes including *GALEX* MIS, VST KiDS, VISTA VIKING, *WISE*, *Herschel*-ATLAS, GMRT, and ASKAP providing UV to radio coverage. GAMA is funded by the STFC (UK), the ARC (Australia), the AAO, and the participating institutions. The GAMA website is http://www.gama-survey.org/.

APPENDIX A
X-RAY CLUSTERS

The *Chandra* clusters from Section 6.2.1 are described in Table 3 and the XCS clusters from Section 6.2.2 are described in Table 4.

Table 10

redMaPPer z_{max} Map Format

Name	Format	Description
HPIX[a]	INT(8)	HEALPIX ring-ordered pixel number
ZMAX	FLOAT(4)	Maximum redshift of a cluster centered in this pixel
FRACGOOD	FLOAT(4)	Fraction of pixel area that is not masked

Note.
[a] We use NSIDE=4096 for the SVA1 catalogs, and NSIDE=2048 for the DR8 catalog.

Table 11
redMaPPer Random Points Catalog Format

Name	Format	Description
R.A.	FLOAT(8)	R.A. in decimal degrees (J2000)
decl.	FLOAT(8)	decl. in decimal degrees (J2000)
Z	FLOAT(4)	Redshift of random point
LAMBDA	FLOAT(4)	Richness of random point
WEIGHT	FLOAT(4)	Weight of random point

Table 12
redMaPPer Effective Area Format

Name	Format	Description
Z	FLOAT(4)	Redshift cut
AREA	FLOAT(4)	Effective area

APPENDIX B
DATA CATALOG FORMATS

The full redMaPPer SDSS DR8 and DES SVA1 catalogs will be available at http://risa.stanford.edu/redmapper/in FITS format, and the DES SVA1 catalogs at http://des.ncsa.illinois.edu/releases/sva1. The catalogs will also be available from the journal. A summary of all of the data tables provided is shown in Table 5, with pointers to the associated tables which describe the data products. Note that there are two versions of the SVA1 catalog—the fiducial catalog, and the expanded-footprint catalog with inferior star/galaxy separation and less aggressive masking. The cluster ID numbers are not matched between these two versions of the catalog, which are considered distinct.

REFERENCES

Ahn, C. P., Alexandroff, R., Allende Prieto, C., et al. 2014, ApJS, 211, 17
Aihara, H., Allende Prieto, C., An, D., et al. 2011, ApJS, 193, 29
Akritas, M. G., & Bershady, M. A. 1996, ApJ, 470, 706
Allen, S. W., Evrard, A. E., & Mantz, A. B. 2011, ARA&A, 49, 409
Arnaud, K. A. 1996, in ASP Conf. Ser. 101, Astronomical Data Analysis Software and Systems V, ed. G. H. Jacoby, & J. Barnes (San Francisco, CA: ASP), 17
Arnaud, M., Pointecouteau, E., & Pratt, G. W. 2005, A&A, 441, 893
Ascaso, B., Wittman, D., & Benítez, N. 2012, MNRAS, 420, 1167
Ascaso, B., Wittman, D., & Dawson, W. 2014, MNRAS, 439, 1980
Becker, M. R., Troxel, M. A., MacCrann, N., et al. 2015, arXiv:1507.05598
Benson, B. A., de Haan, T., Dudley, J. P., et al. 2013, ApJ, 763, 147
Bertin, E. 2011, in ASP Conf. Ser. 442, Astronomical Data Analysis Software and Systems XX, ed. I. N. Evans et al. (San Francisco, CA: ASP), 435
Bertin, E., & Arnouts, S. 1996, A&AS, 117, 393
Bleem, L. E., Stalder, B., de Haan, T., et al. 2015, ApJS, 216, 27
Bocquet, S., Saro, A., Mohr, J. J., et al. 2015, ApJ, 799, 214
Bruzual, G., & Charlot, S. 2003, MNRAS, 344, 1000
Chang, C., Busha, M. T., Wechsler, R. H., et al. 2015a, ApJ, 801, 73
Chang, C., Vikram, V., Jain, B., et al. 2015b, PhRvL, 115, 051301
Clerc, N., Sadibekova, T., Pierre, M., et al. 2012, MNRAS, 423, 3561
Colless, M., Dalton, G., Maddox, S., Sutherland, W. & the 2dF collaboration 2001, MNRAS, 328, 1039
Cooper, M. C., Yan, R., Dickinson, M., et al. 2012, MNRAS, 425, 2116
Dawson, K. S., Schlegel, D. J., Ahn, C. P., et al. 2013, AJ, 145, 10
de Jong, J. T. A., Verdoes Kleijn, G. A., Boxhoorn, D. R., et al. 2015, A&A, 582, A62
Desai, S., Armstrong, R., Mohr, J. J., et al. 2012, ApJ, 757, 83
Dickey, J. M., & Lockman, F. J. 1990, ARA&A, 28, 215
Driver, S. P., Hill, D. T., Kelvin, L. S., et al. 2011, MNRAS, 413, 971
Eddington, A. S. 1913, MNRAS, 73, 359
Eisenstein, D. J., Annis, J., Gunn, J. E., et al. 2001, AJ, 122, 2267
Evrard, A. E., Arnault, P., Huterer, D., & Farahi, A. 2014, MNRAS, 441, 3562
Fioc, M., & Rocca-Volmerange, B. 1997, A&A, 326, 950
Flaugher, B., Diehl, H. T., Honscheid, K., et al. 2015, AJ, 150, 150
Fruscione, A., McDowell, J. C., Allen, G. E., et al. 2006, in Society of Photo-Optical Instrumentation Engineers (SPIE) Conference Series, Vol. 6270, Society of Photo-Optical Instrumentation Engineers (SPIE) Conference Series, 1
Garilli, B., Guzzo, L., Scodeggio, M., et al. 2014, A&A, 562, A23
Garilli, B., Le Fèvre, O., Guzzo, L., et al. 2008, A&A, 486, 683
Gladders, M. D., Yee, H. K. C., Majumdar, S., et al. 2007, ApJ, 655, 128
Górski, K. M., Hivon, E., Banday, A. J., et al. 2005, ApJ, 622, 759
Goto, T., Sekiguchi, M., Nichol, R. C., et al. 2002, AJ, 123, 1807
Hansen, S. M., Sheldon, E. S., Wechsler, R. H., & Koester, B. P. 2009, ApJ, 699, 1333
Hao, J., Koester, B. P., Mckay, T. A., et al. 2009, ApJ, 702, 745
Hao, J., McKay, T. A., Koester, B. P., et al. 2010, ApJS, 191, 254
Hasselfield, M., Hilton, M., Marriage, T. A., et al. 2013, JCAP, 7, 8
Henry, J. P., Evrard, A. E., Hoekstra, H., Babul, A., & Mahdavi, A. 2009, ApJ, 691, 1307
Hoffleit, D., & Jaschek, C. 1991, The Bright Star Catalogue (5th ed.; New Haven, CT: Yale Univ. Observatory)
Jarvis, M., Sheldon, E., Zuntz, J., et al. 2015, arXiv:1507.05603
Johnston, D. E., Sheldon, E. S., Wechsler, R. H., et al. 2007, arXiv:0709.1159
Kelly, P. L., von der Linden, A., Applegate, D. E., et al. 2014, MNRAS, 439, 28
Koester, B. P., McKay, T. A., Annis, J., et al. 2007a, ApJ, 660, 239
Koester, B. P., McKay, T. A., Annis, J., et al. 2007b, ApJ, 660, 221
Laureijs, R., Amiaux, J., Arduini, S., et al. 2011, arXiv:1110.3193
Leistedt, B., Peiris, H. V., Elsner, F., et al. 2015, arXiv:1507.05647
Lieu, M., Smith, G. P., Giles, P. A., et al. 2015, arXiv:1512.03857
Lloyd-Davies, E. J., Romer, A. K., Mehrtens, N., et al. 2011, MNRAS, 418, 14 (LD11)
LSST Science Collaboration, Abell, P. A., Allison, J., et al. 2009, arXiv:0912.0201
Mancone, C. L., & Gonzalez, A. H. 2012, PASP, 124, 606
Mantz, A., Allen, S. W., Rapetti, D., & Ebeling, H. 2010, MNRAS, 406, 1759
Mehrtens, N., Romer, A. K., Hilton, M., et al. 2012, MNRAS, 423, 1024
Melchior, P., Suchyta, E., Huff, E., et al. 2015, MNRAS, 449, 2219
Mewe, R., Gronenschild, E. H. B. M., & van den Oord, G. H. J. 1985, A&AS, 62, 197
Murphy, D. N. A., Geach, J. E., & Bower, R. G. 2012, MNRAS, 420, 1861
Navarro, J. F., Frenk, C. S., & White, S. D. M. 1994, MNRAS, 267, L1
Oguri, M. 2014, MNRAS, 444, 147
Old, L., Wojtak, R., Mamon, G. A., et al. 2015, MNRAS, 449, 1897
Planck Collaboration, Ade, P. A. R., Aghanim, N., et al. 2014, A&A, 571, A20
Planck Collaboration, Ade, P. A. R., Aghanim, N., et al. 2015, arXiv:1502.01598
Reyes, R., Mandelbaum, R., Hirata, C., Bahcall, N., & Seljak, U. 2008, MNRAS, 390, 1157
Rozo, E., & Rykoff, E. S. 2014, ApJ, 783, 80 (RM2)
Rozo, E., Rykoff, E. S., Abate, A., et al. 2015c, arXiv:1507.05460 (RM15)
Rozo, E., Rykoff, E. S., Bartlett, J. G., & Melin, J.-B. 2015a, MNRAS, 450, 592 (RM3)
Rozo, E., Rykoff, E. S., Becker, M., Reddick, R. M., & Wechsler, R. H. 2015b, MNRAS, 453, 38 (RM4)
Rozo, E., Rykoff, E., Koester, B., et al. 2011, ApJ, 740, 53
Rozo, E., Rykoff, E. S., Koester, B. P., et al. 2009, ApJ, 703, 601
Rozo, E., Wechsler, R. H., Rykoff, E. S., et al. 2010, ApJ, 708, 645
Rykoff, E. S., Rozo, E., & Keisler, R. 2015, arXiv:1509.00870
Rykoff, E. S., Koester, B. P., Rozo, E., et al. 2012, ApJ, 746, 178
Rykoff, E. S., Rozo, E., Busha, M. T., et al. 2014, ApJ, 785, 104 (RM1)
Sadibekova, T., Pierre, M., Clerc, N., et al. 2014, A&A, 571, A87
Saro, A., Bocquet, S., Rozo, E., et al. 2015, MNRAS, 454, 2305 S15

Schellenberger, G., Reiprich, T. H., Lovisari, L., Nevalainen, J., & David, L. 2015, A&A, 575, A30
Scoville, N., Aussel, H., Brusa, M., et al. 2007, ApJS, 172, 1
Sevilla, I., Armstrong, R., Bertin, E., et al. 2011, arXiv:1109.6741
Sinnott, R. W. 1988, The Complete New General Catalogue and Index Catalogues of Nebulae and Star Clusters, ed. J. L. E. Dreyer (Cambridge: Cambridge Univ. Press)
Skrutskie, M. F., Cutri, R. M., Stiening, R., et al. 2006, AJ, 131, 1163
Soares-Santos, M., de Carvalho, R. R., Annis, J., et al. 2011, ApJ, 727, 45
Swanson, M. E. C., Tegmark, M., Hamilton, A. J. S., & Hill, J. C. 2008, MNRAS, 387, 1391
Szabo, T., Pierpaoli, E., Dong, F., Pipino, A., & Gunn, J. 2011, ApJ, 736, 21
The Dark Energy Survey Collaboration, Abbott, T., Abdalla, F. B., et al. 2015, arXiv:1507.05552
The DES Collaboration 2005, arXiv:0510346
Tinker, J., Kravtsov, A. V., Klypin, A., et al. 2008, ApJ, 688, 709
Vikhlinin, A., Kravtsov, A. V., Burenin, R. A., et al. 2009, ApJ, 692, 1060
Vikram, V., Chang, C., Jain, B., et al. 2015, PhRvD, 92, 022006
Weinberg, D. H., Mortonson, M. J., Eisenstein, D. J., et al. 2013, PhR, 530, 87
Wen, Z. L., Han, J. L., & Liu, F. S. 2012, ApJS, 199, 34
York, D. G., Adelman, J., Anderson, J. E., Anderson, S. F., Annis, J. & the SDSS collaboration 2000, AJ, 120, 1579
Yuan, F., Lidman, C., Davis, T. M., et al. 2015, MNRAS, 452, 3047